JACS JOURNAL OF THE AMERICAN CHEMICAL SOCIETY

Article

pubs.acs.org/JACS

Control of Reactivity and Regioselectivity for On-Surface Dehydrogenative Aryl−Aryl Bond Formation

Nemanja Kocić,*[†] Xunshan Liu,[‡] Songjie Chen,[‡] Silvio Decurtins,[‡] Ondřej Krejčí,[§,∥] Pavel Jelínek,[§] Jascha Repp,[†] and Shi-Xia Liu*[‡]

[†]Institute of Experimental and Applied Physics, University of Regensburg, 93053 Regensburg, Germany

[‡]Department of Chemistry and Biochemistry, University of Bern, 3012 Bern, Switzerland

[§]Institute of Physics of Czech Academy of Sciences, 16200 Prague, Czech Republic

[∥]Charles University in Prague, Faculty of Mathematics and Physics, Department of Surface and Plasma Science, 18000 Prague, Czech Republic

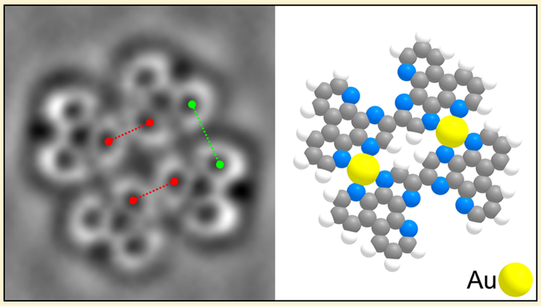

ABSTRACT: Regioselectivity is of fundamental importance in chemical synthesis. Although many concepts for site-selective reactions are well established for solution chemistry, it is not *a priori* clear whether they can easily be transferred to reactions taking place on a metal surface. A metal will fix the chemical potential of the electrons and perturb the electronic states of the reactants because of hybridization. Additionally, techniques to characterize chemical reactions in solution are generally not applicable to on-surface reactions. Only recent developments in resolving chemical structures by atomic force microscopy (AFM) and scanning tunneling microscopy (STM) paved the way for identifying individual reaction products on surfaces. Here we exploit a combined STM/AFM technique to demonstrate the on-surface formation of complex molecular architectures built up from a heteroaromatic precursor, the tetracyclic pyrazino[2,3-*f*][4,7]phenanthroline (**pap**) molecule. Selective intermolecular aryl−aryl coupling via dehydrogenative C−H activation occurs on Au(111) upon thermal annealing under ultrahigh vacuum (UHV) conditions. A full atomistic description of the different reaction products based on an unambiguous discrimination between pyrazine and pyridine moieties is presented. Our work not only elucidates that *ortho*-hydrogen atoms of the pyrazine rings are preferentially activated over their pyridine equivalents, but also sheds new light onto the participation of substrate atoms in metal−organic coordination bonding during covalent C−C bond formation.

■ INTRODUCTION

There are many synthetic protocols for the aryl−aryl bond formation, among which palladium-catalyzed cross-coupling chemistry is certainly most prominent in organic chemistry.[1] Nevertheless, the dehydrogenation, for instance between contiguous phenyls in phenylbenzenes, plays a similarly important role.[2] Notably the Scholl reaction,[3] the dehydrogenative coupling under the influence of a Lewis acid, has often been used for polyphenylene compounds, which are further converted to the corresponding polycyclic aromatic hydrocarbons (PAHs). These solution-based protocols paved the way for the preparation of a wide variety of π-extended PAHs by employing tailor-made oligophenylene precursors.[4] In a similar vein, noteworthy studies assessed whether the corresponding reaction mechanisms are based on the generation of a radical cation or an arenium cation. For example, Butenschön et al. initiated a discussion on the comparison of oxidative aromatic coupling and the Scholl reaction aiming to encourage further mechanistic studies.[5] Much less is known about a systematic examination on heterocyclic systems. Representative examples were exemplified by preparation of on N-doped nanographenes and graphene nanoribbons via cyclodehydrogenation of a dipyrimidyl-substituted precursors.[6]

In contrast to the solution-based method, a complementary on-surface synthesis under UHV conditions enables the realization of unprecedented structures of PAHs that are otherwise unattainable.[7] A specific underlying growth mechanism has been described by Cai et al.[8] It demonstrates the occurrence of an Au(111) surface-assisted dehalogenation reaction of dibromo-bianthryl (C−C bond formation by Ullmann coupling) leading to linear polyphenylene chains at 200 °C which undergo a cyclodehydrogenation process upon annealing to 400 °C, yielding structurally perfect and fully π-conjugated carbon nanoribbons. Depending on the precursor molecules, on-surface preparation of this type provides access to graphene nanoribbons with different widths and edge structures,[9] including heteroatom-doped ones.[10] An intriguing question is, however, how a specific atomic configuration between reactant and metal catalyst controls the reaction process. In response, a recent study focused on the

Received: December 24, 2015
Published: April 8, 2016

DOI: 10.1021/jacs.5b13461
J. Am. Chem. Soc. 2016, 138, 5585−5593

dehalogenation and C−C coupling mechanisms of a polycyclic hydrocarbon compound on a metal substrate covered with a monolayer of hexagonal boron-nitride.[11] To summarize, a key insight from on-surface reactions is, that there are no inherent limitations for this strategy to be extended to more complex systems, as far as the necessary precursor monomers can be synthesized. In practical terms, however, finding new routes to fabricate complex heterostructures with for instance atomically precise N/C locations, still remains a challenge.[12]

A further important point is that the work, hitherto reported, does not yet adequately account for the possibility to steer catalytic regioselectivity,[13] means to favor bond formation at a particular atom over other possible atoms, into the class of surface-assisted reactions. The on-surface C−H bond scission is generally not regiospecific when the molecules contain several C−H bonds.[14] Very recently, one approach is given with an experimental and theoretical study on cyclodehydrogenation reactions of tetraphenylporphyrin (2H-TPP) molecules on Ag(111). It has been found that the 2-fold symmetry of the 2H-TPP's core, which is defined by the position of the H atoms, determines the selective reaction outcome.[13a] An alternative path for the regioselective formation of sophisticated structures is to apply a step-by-step connection of molecules which allows to connect them in a hierarchical manner by a selective and sequential activation of different sites on their perimeter.[15] To achieve selectivity, these reactive sites must be incorporated in the initial molecular building block. In conjunction with the catalytic selectivity issue, the work of Hanke et al. draws our attention to cooperative effects. Cyclodehydrogenation corresponds to positive cooperativity; hence, the probability of any given coupling is drastically increased if a neighboring coupling already exists.[16]

An important consensus is that significant progress in the field of on-surface synthesis has mainly been facilitated by single-molecule characterization techniques such as atomic force microscopy (AFM) and scanning tunneling microscopy (STM). Recently, the chemical structures of individual molecules have been resolved by AFM which was enabled by the functionalization of the tip.[17] This method has paved the way of identifying individual molecules on surfaces in various contexts,[18] and was soon after applied to in situ characterize and visualize on-surface chemical reaction products.[19]

In continuation of our current research focus on fused heterocyclic compounds[20] such as tetraazaperylene,[21] we set out to probe an even smaller tetraazapolycyclic precursor molecule, pyrazino[2,3-*f*][4,7]phenanthroline (**pap**),[22] for selective on-surface dehydrogenation and subsequent intermolecular C−C bond formation. This planar bis-N^N chelating molecule (Scheme 1) has so far exclusively been studied in the field of coordination chemistry acting as a bridging ligand to transition metal ions.[23] However, this heterocyclic molecule did draw our attention, first because its eight C−H bonds could be potentially differentiated in the dehydrogenative reaction pathways. Since two hydrogen atoms on the pyrazine ring may preferentially be activated over their pyridine equivalents, selective reaction sites are inherently incorporated. Second, subsequent intermolecular C−C bond formation can lead to larger heterocyclic compounds revealing atomically precise N/C locations. Here we present a combined STM/AFM investigation of an on-surface chemical reaction of the **pap** molecule under UHV conditions. This work demonstrates a clear discrimination between pyrazine and pyridine rings of the reaction products, thus giving convincing support for pyrazines' inherent reactivity playing a key role in the regioselective aryl−aryl dehydrogenative coupling.

Scheme 1. Molecular Structure of Pyrazino[2,3-*f*][4,7]phenanthroline (pap) with Atom Numbering[a]

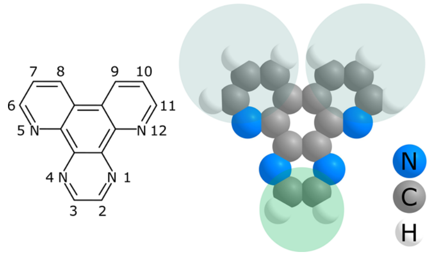

[a]Highlighting examples of potential sites for selective intermolecular C−C couplings via on-surface dehydrogenation.

MATERIALS AND METHODS

Chemicals. Pyrazino[2,3-*f*][4,7]phenanthroline (**pap**) was synthesized as described previously.[22] The high yield is in the range of 80−90%.

STM/AFM Measurements. The experiments were carried out with a home-built combined STM/AFM operated in ultrahigh vacuum at a sample temperature of 6 K. The AFM is based on a qPlus tuning fork design (resonance frequency $f_0 = 28.67$ kHz, spring constant $k_0 \approx 1.8 \times 10^3$ N/m, quality-factor $Q \approx 10^4$, oscillation amplitude $A_{osc} = 50$ pm,[24] and was operated in frequency-modulation mode. For FM-AFM measurements, the apex of the tip was functionalized with a CO molecule and the images were recorded at sample bias $V = 0$ V by measuring the frequency shift while scanning in constant-height mode. After preparing a clean Au(111) surface from cyclic sputtering and annealing to 550 °C, **pap** molecules were deposited at a sample temperature below 10 K.

Simulations. The calculations of the free-standing molecules have been performed within the density functional theory (DFT) as implemented in the SIESTA code.[25] The calculations are based on both the local-density approximation (LDA) and the generalized gradient approximation (GGA). Core electrons are replaced by nonlocal norm-conserving pseudopotentials and valence electrons are described by linear combinations of numerical pseudoatomic orbitals. An energy cutoff of 400 Ry is employed and a double-ζ plus polarization basis set is used for the basis orbitals.

In addition, we performed total-energy DFT calculations using the FHI-aims code[26] to determine the adsorption geometry of **pap** molecules on a Au(111) surface. We carried out slab calculations: for the **pap** dimers optimization we employed a 8 × 8 supercell made of four Au layers to describe the Au(111) surface. From these, the three lower-most Au layers were kept fixed. A relaxation procedure was performed until the remaining atomic forces and changes of the total-energy were below 10^{-2} eV/Å and 10^{-5} eV, respectively. Only the Gamma point was used for the integration in the Brillouin zone. All the calculations were carried out at the GGA-PBE level including the Tkatchenko−Scheffler[27] treatment of the Van-der-Waals interactions.

To simulate the high-resolution AFM images, we used a mechanical probe-particle AFM model[28] including the electrostatic interaction.[29] The frequency shift was computed from the simulated $F(z)$-curves using Giessibl's formula[30] using the experimental values of $A_{osc} = 50$ pm, $k_0 \approx 1.8 \times 10^3$ N/m and a lateral stiffness of the CO molecule of 0.5 N/m with an effective charge on the probe particle of −0.05 elementary charges (which is in agreement with our previously published results).

RESULTS AND DISCUSSION

The **pap** molecule was structurally characterized by single crystal X-ray measurement from its hydrated solid.[23c] It is virtually planar; the maximum atomic deviation from the least-

DOI: 10.1021/jacs.5b13461
J. Am. Chem. Soc. 2016, 138, 5585−5593

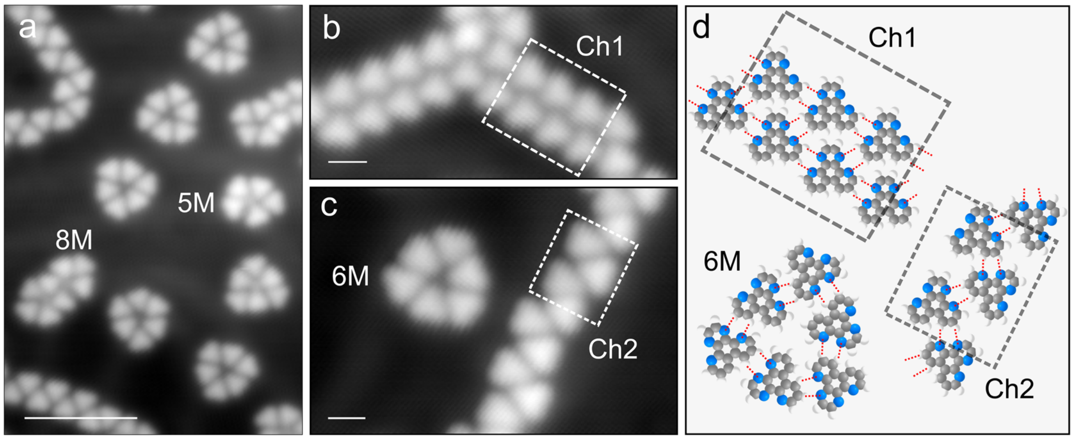

Figure 1. STM measurements of self-assembled hydrogen-bonded structures of pap molecules. (a−c) Typical self-assembled molecular clusters and (d) their proposed structure models with the same color code as in Scheme 1. Imaging parameters: $V = 0.3$ V, $I = 2$ pA. Scale bar: (a) 5 nm and (b,c) 1 nm.

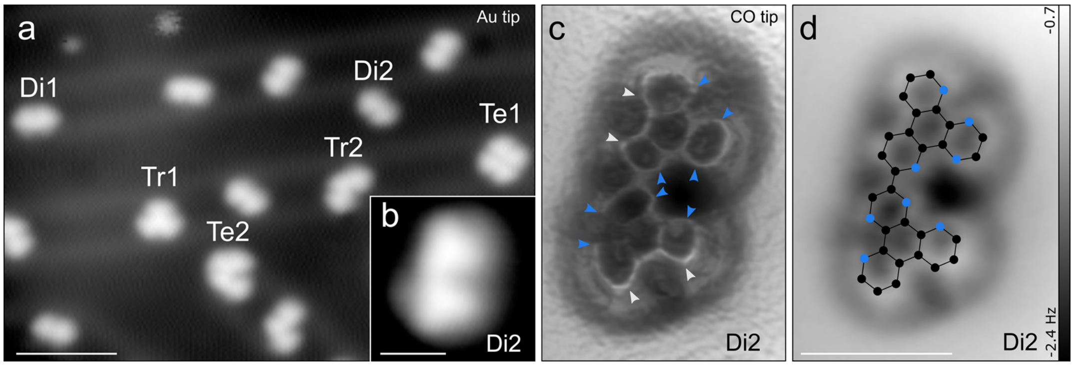

Figure 2. STM/AFM measurements of covalently bonded structures. (a) STM image showing several different dimer (Di1, Di2), trimer (Tr1, Tr2), and tetramer (Te1, Te2) structures. (b) STM image of one of a Di2-dimer structure. (c and d) AFM images of the same Di2-dimer as shown in (b). The same AFM-image is displayed twice with (c) and without (d) being high-pass filtered to highlight the molecular structure. The two **pap** molecules constituting the dimer can be readily identified. The distances between each two marked (arrow heads) atoms in every edge of the molecules appear quite differently in the images. From this, the carbon (long apparent distance, C8−C9, white) and nitrogen (short apparent distance, N4−N5 and N1−N12, blue) can be identified. On the basis of this identification the position of the edges including the nitrogen atoms can be identified from STM images as the ones exhibiting a smoother contrast transition. In (d) the resulting molecular structure is overlaid with black and blue circles as carbons and nitrogens, respectively. Imaging parameters: (a) $V = 0.3$ V, $I = 1$ pA. (b) $V = 0.05$ V, $I = 1$ pA. (c,d) $\Delta z = 1.33$ Å, Δz corresponds to a distance decrease with respect to a STM set point of $I = 1$ pA, $V = 0.05$ V above the clean Au surface. Scale bar: (a) 5 nm and (b,d) 1 nm.

squares plane is 0.098 Å and the mean deviation is 0.05 Å. First, the self-assembly behavior of **pap** on the Au(111) surface was investigated. The molecules were deposited at a substrate temperature below 10 K and the sample surface was imaged after an annealing step to room temperature. As illustrated in Figure 1, STM images of the surface show an average coverage of approximately one molecule per 3 nm^2. As is immediately apparent, the molecules form different types of self-assembled structures, including small clusters but also longer chains of molecules. While the self-assembled structure formation is not the focus of this work, this observation proves that even at room-temperature the molecules have enough mobility to aggregate in self-assembled structures. All structures can be rationalized in terms of C−H···N hydrogen bonds formed between neighboring molecules.

To initiate the on-surface reaction, we annealed the sample to (410 ± 25) °C for 1 min. Figure 2a shows a typical STM image of the surface after the annealing. From this and many other STM images in total 166 clusters were observed. Six different types of clusters, namely dimers (Di1, Di2), trimers (Tr1, Tr2), and tetramers (Te1, Te2) make up 94% of all structures, while no remaining monomers could be found on the surface. The limited size of clusters is in stark contrast to the self-assembled structures studied before the annealing step and a first hint toward the regioselectivity of the reaction. If all of the hydrogen sites would show the same reactivity, there would be no reason that no larger structures are formed as seen in the self-assembled structures. However, if one assumes that dehydrogenation mainly occurs at the pyrazine moiety of the molecule, clusters of limited size can be expected.

To gain information about the regioselectivity from AFM in real space, one has to be able to identify the different sites within the molecule; in the actual context a discrimination of pyridine from pyrazine is necessary. Whereas for phenazine adsorbed on a copper surface the nitrogen can readily be identified inside the molecule,[19a] this is not directly apparent in the present case. That the substrate may affect the appearance of atoms in adsorbed molecules in AFM images goes in line with simulations of the AFM-imaging process performed for graphene nanoribbons doped with boron atoms.[31] There it was

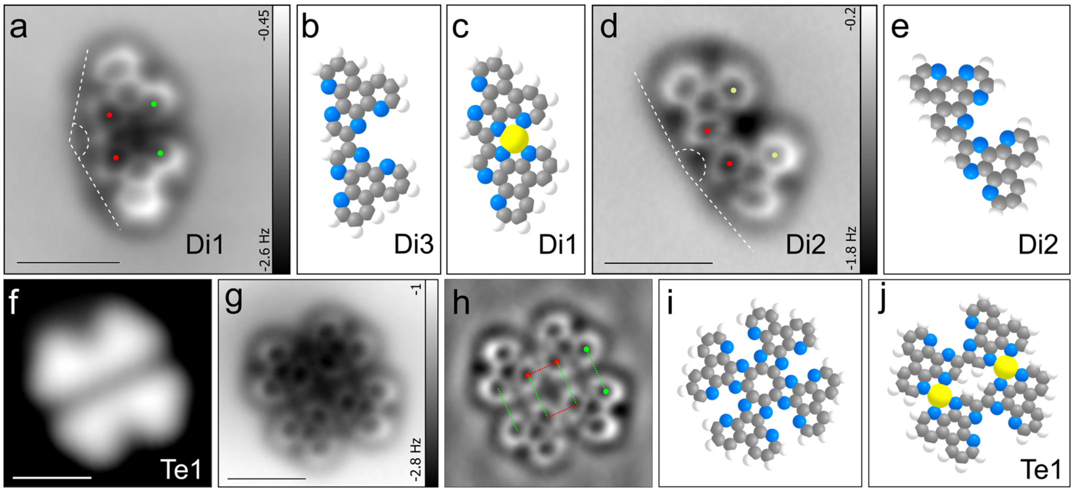

Figure 3. Detailed analysis of some of the observed molecular structures. (a and d) AFM images of a Di1- and a Di2-dimer, respectively. The distances between adjacent heterocycles (red and green dots) indicates that only one covalent bond was formed between each two **pap** constituents. The corresponding distance (red dots) of about 0.42 nm is in very good agreement to the distance expected for such a covalent bond. The main difference between the two dimer structures lies in the bond that has formed upon annealing (C2-to-C2 vs C2-to-C6). Another characteristic difference between the two dimer structures is the angle of alignment of the two **pap** constituents as indicated by the dashed lines in the images. Whereas the alignment in Di2 is consistent with just a covalent bond formation, the alignment observed in Di1 can only be rationalized if a stabilization of the dimer via metal coordination bonds is assumed, as shown in (c). Hence, the slightly shorter distance between adjacent heterocycles (green dots) of about 0.50 nm compared to the one of about 0.72 nm (yellow dots) we interpret as being indicative of a metal coordination bond being present. The appearance of the molecular structure allows one to identify the nitrogen atoms (see above) as shown in the corresponding models (b, c, and e). (f−j) STM (f), AFM (g), high-pass filtered AFM (h) image and structural models (i, j) of the Te1 tetramer. Based on the dimer analysis one readily observes distinctly different distances between adjacent heterocycles in Te1, indicating that Te1 consists of two dimer structures that are interconnected by metal coordination bonds to form the tetramer as illustrated in (j). Other possible structures as the one in (i) do not reproduce the distances and alignment angles of Te1. Imaging parameters: (a,d) Δz = 1.33 Å from V = 0.05 V, I = 1 pA. (g) Δz = 1.9 Å from V = 0.2 V, I = 1 pA. (f) STM image V = 0.2 V, I = 1 pA. Scale bars: 1 nm.

claimed that the difference in AFM contrast on boron atoms is only due to their different adsorption height as compared to carbon atoms. On the less reactive surface of Au(111) used here, it is therefore not surprising that no clear difference is observed. Nevertheless, the nitrogen sites can also be identified in the present case by two observations as follows.

Within the triphenylene backbone of the **pap** molecule at four of six distinct atomic positions the nitrogen atoms are incorporated. The C8−C9 distance is slightly larger than the N4−N5 and N1−N12. On top, image distortions in AFM imaging with CO functionalized tips may influence the apparent atomic distances.[32] Important in the current context is the prediction that electrostatic interactions contribute considerably to these distortions.[28] As the C−N bonds inside the molecule are expected to be slightly polar, AFM image distortions should slightly differ at the nitrogen and carbon positions in molecules. The distances between each two of these atomic positions in every edge of the molecules (see Figure 2c) appear quite differently in the images. The distance in one edge is particularly longer (3.5−4.0 Å) than those in the two other edges (2.3−2.9 Å). From this observation, the carbon (long apparent distance between C8−C9, white arrowheads) and nitrogen (short apparent distance between N4−N5 and N1−N12, blue arrowheads) can be identified. This assignment is supported by DFT calculations and AFM image simulations as will be discussed further below.

In STM images, each molecule appears as a triangular protrusion. When directly relating the STM and AFM images of the same individual structures, one realizes that the nitrogen-substituted edges - as determined from the AFM distortions - appear smoother than the ones without nitrogen. Whereas at one of its three edges the contrast falls off relatively abruptly, at the two other sides this transition is smoother. This correlation between STM contrast and AFM-image distortions further supports the assignment of nitrogen positions inside the molecules.

Being able to identify the positions of nitrogens as discussed above, we now turn to the discussion of bond formation in different structures. From atomically resolved AFM images we extracted structural information, namely, which intermolecular chemical bonds were formed. Figure 3a−e show the analysis of dimer structures. Irrespective of the AFM contrast indicating a covalent bond, the distances between adjacent heterocycles can be used as an indication of whether or not a bond is formed. The corresponding distance (red dots in Figure 3a,d) of (0.42 ± 0.03) nm is in excellent agreement to the distance expected for such a covalent bond. DFT calculations of the covalently bonded dimer structure without substrate yield the same distance of 0.42 nm. Both dimer structures indicate that only one covalent bond per dimer has been formed. In Di1 a bond has formed between two pyrazine moieties, namely a C2-to-C2-bond, according to the numbering introduced in Scheme 1. Di2, in contrast, involves a bond between a pyrazine and a pyridine moiety, a C2-to-C6-bond. We counted 101 dimers of type Di1 and 20 dimers of Di2 in our study, indicating the preference for pyrazine-bonded structures. Another characteristic difference between the two dimer structures is the alignment of the two **pap** constituents as indicated in Figure 3. Whereas the alignment in Di2 is consistent with just a covalent bond formation, the alignment observed in Di1 suggests that the different angle is due to a stabilization of the dimer via metal coordination bonding, as shown in Figure 3c. To corroborate this interpretation, we also performed DFT calculations of these structures, again excluding the substrate.

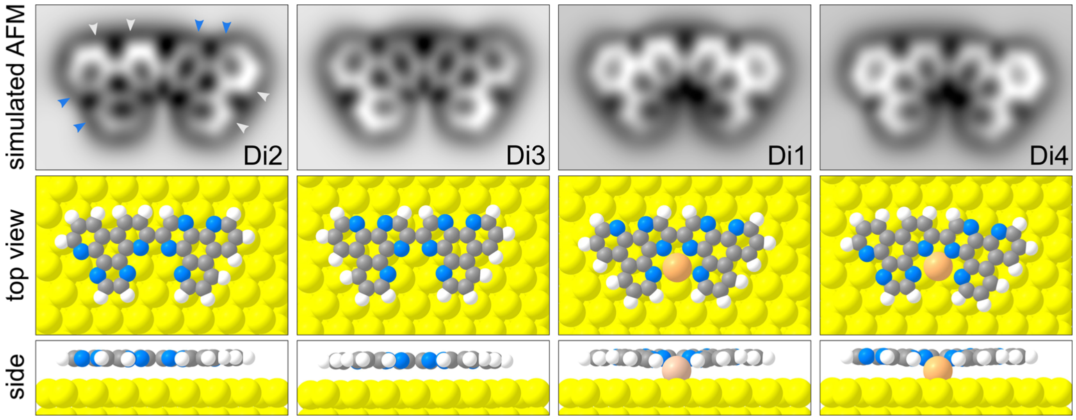

Figure 4. DFT-calculated structures and simulated AFM images. Pyrazine−pyrazine (C2-to-C2-bond, D1 and Di3) and pyrazine−pyridine (C2-to-C6-bond, Di2 and Di4) dimers, each with (Di1, Di4) and without (Di2, Di3) a gold adatom coordinated to nitrogens are shown in the calculated geometries. The corresponding simulated AFM images are shown above. The difference in the C8−C9 versus N4−N5 or N1−N12 distances (white and blue arrowheads, respectively) confirm the experimental assignment.

The DFT calculations reproduce the observed alignment angles (see Figure 3a,d) only if one includes or excludes a coordinating gold atom for Di1 and Di2, respectively. In particular, the slightly larger distance between the adjacent heterocycles that are not covalently bonded to each other (green dots in Di1) of (0.50 ± 0.03) nm is in qualitative agreement with the corresponding simulated structure (see Figure 3c). In contrast, if there is no metal coordination involved, the corresponding distance measures (0.72 ± 0.04) nm (yellow dots). We hence interpret this distance variation as being indicative of a metal coordination bond being present.[33] At first glance it is surprising that the gold atom is not directly visible in the AFM images—a circumstance that will be elucidated further below, after the analysis of tetramer Te1, shown in Figure 3f−j. On the surface it has C_{2v} symmetry (D_{2h} in the gas-phase) indicating that the bonds between the constituents are not all of the same nature. Following the reasoning from the dimer structure as outlined above, one immediately recognizes that Te1 consists of two dimers connected to each other via metal coordination bonds. This hypothesis is supported by DFT calculations carried out for the tetramer Te1 without substrate. Alternate models, e.g., assuming four covalent bonds, do not reproduce the experimentally observed structure.

We performed total-energy DFT calculations of four selected dimer structures including the substrate. Next we calculated AFM images of the corresponding optimized structures (see upper panel of Figure 4). Note that the image simulations take into account the bending of the CO molecule at the tip apex,[28,34] while the parameters required to simulate a CO tip were selected upon previous image simulations and their direct comparison to experimental data in other works.[35] To understand the possible participation of gold adatoms in metal−organic coordination bonding in our structures, we calculated not only Di1 and Di2, but two more dimers: The counterpart of Di1, but without a gold atom, henceforth labeled Di3, and the counterpart of Di2, but with an additional gold adatom, henceforth labeled Di4. Hence, these structures are pyrazine−pyrazine (C2-to-C2-bond, Di1 and Di3) and pyrazine−pyridine-bonded (C2-to-C6-bond, Di4 and Di2) dimers, each with and without a gold adatom coordinated to nitrogens. The relaxed geometries are shown in Figure 4, alongside with simulated AFM images. First we turn to the discussion of C8−C9 versus N4−N5 and N1−N12 distances, relevant for the assignment of nitrogen positions in each molecule. The DFT calculation yields C8−C9-distances of 2.98−3.00 Å being distinctly larger than the N4−N5 and N1−N12 distances that measure only 2.69−2.78 Å. In the AFM imaging with a CO-terminated tip, this difference seems to be even exaggerated by distortions, such that in the simulated images it can be clearly discerned (see white and blue arrowheads) in agreement with the experiment. This puts the assignment of nitrogen positions inside the molecules from AFM images onto solid grounds.

The simulated images also confirm that it is possible to have a coordinating gold atom present in the structure without directly resolving it with the AFM as a repulsive feature. The reason for the absence of a repulsive feature from the gold adatom is related to (i) presence of charge transfer between the gold adatom and the molecule giving rise to an additional attractive interaction with CO-tip and to (ii) the vertical position of the gold adatom and the surrounding nitrogen atoms being considerably closer to the surface than the one of the organic framework, diminishing the onset of Pauli repulsion. Consequently, the gold atom leads to a dark circular halo of long-range attractive interaction. Indeed such a dark halo can also be seen in the experimental AFM image of Di1, for which we expect a gold adatom to be present, lending further support for the presence of a gold adatom.

What more, both dimer structures without gold adatom show a straight 180° alignment angle consistent with our interpretation of Di2. However, the angle of Di1 is about 170°, but not as small as the experimentally observed one. We also note that the experimental image of Di1 has a bright protrusion at the bond that formed upon annealing, which is not reproduced by the calculated AFM image, leaving some room for the interpretation of the atomistic details in Di1, in particular as it regards the exact position and bonding of an additional gold atom. We therefore conclude that the exact bonding geometry in Di1 is not fully captured by our DFT calculation. This can be ascribed to a deficiency in the description of metal−organic complexes by the DFT method.

In addition, we enforced alignment angles smaller than 180° for both, Di1 and Di3. We observed a considerable increase of the total-energy for both structures of few eV for angles smaller than 150°. We therefore exclude that the relatively weak

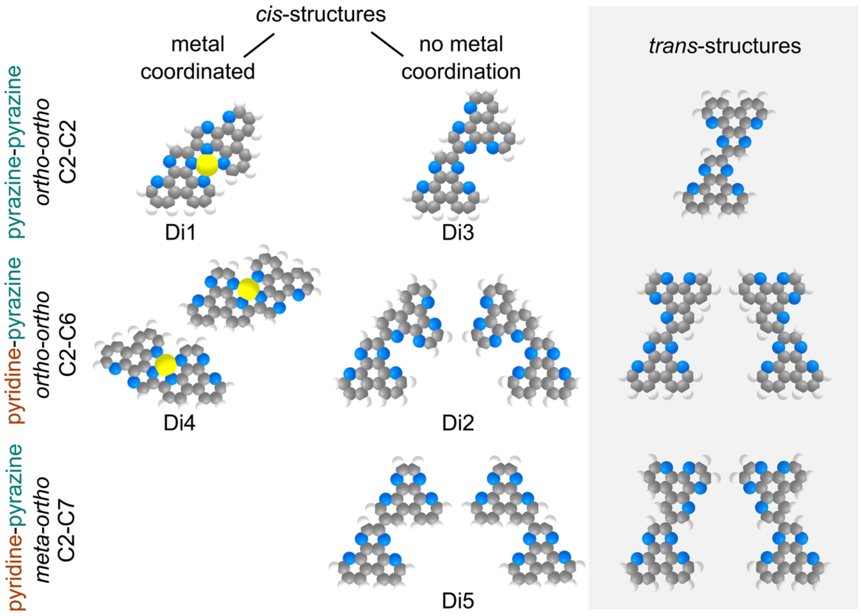

Figure 5. Possible structures of dimer formation. A covalent bond is formed either between *ortho*-carbon atoms of two pyrazine moieties (top row) or between a pyridine and a pyrazine moiety (center row) of the neighboring **pap** molecules. For the pyridine moiety also *meta*- and *para*-carbon atoms exist, which could react to form additional dimer structures exemplified for the *meta*-carbon (bottom row). For the pyridine-bonded structures, there are two enantiomers in each case. The bond configuration can be divided into *cis*-N^N and *trans*-N^N structures. Only the purely *ortho*-carbon bonded *cis*-N^N-structures facilitate metal coordination (Di1 and Di4).

interaction with a flat Au(111) surface without adatoms being present can enforce such a geometry. Our DFT calculations of molecules without a gold adatom revealed only weak, mostly van-der-Waals interaction with the Au(111) substrate underneath. Consequently, the molecules Di2 and Di3 adopt an almost planar configuration with the plane of the molecule located approximately 3.3 Å above the Au(111). The absence of a strong chemical bond between the molecule and the substrate exclude strong conformational changes of the molecules caused by the substrate.

Taking all the above observations into consideration, it is clear that the structural information from AFM images is decisive for the identification of all bonding configurations. However, after establishing the direct relationship between the geometric structure deduced from AFM and the appearances in STM images, one can identify the different type of structures also from the STM images alone. We note that this relationship between structure and appearance in STM images was established and confirmed on the basis of atomically resolved AFM images of in total 26 clusters. We therefore included also all highly resolved STM images in the statistical analysis discussed in the remainder of this work.

A covalent bond either between the two pyrazine moieties (Di1) or between a pyrazine and a pyridine moiety (Di2) of each two neighboring molecules was identified. Another difference between Di1 and Di2 lies in the metal coordination. However, irrespective of a possible metal coordination many more possibilities for a bond formation could be expected, even if regioselectivity is taking place. In this spirit, it is interesting to analyze, which dimer structures could possibly form and to compare that with the actual observations. Before doing so, we note that we never observed any structures involving covalent bonds between two pyridine moieties. We therefore largely exclude this possibility from the following discussion.

Figure 5 shows a set of dimer structures that could be envisioned. A covalent bond between pyridine and pyrazine yields a dimer of lower symmetry than in the other case, which therefore may occur in two different enantiomers on the surface. Indeed we observe each two enantiomers in equal amounts within statistical significance. We disregard stereochemistry in the remainder of this work. Moreover, the covalent bond formation could result in either a *cis*-N^N or a *trans*- N^N configuration of the two **pap** constituents as exemplified in Figure 5. Considering the possible stabilization of the *trans*-configuration by intramolecular hydrogen bonds it is most surprising that we never observed any structures in *trans*-configuration of the molecules. This finding can be accounted for the fact that a *trans*-configuration could not be stabilized by a metal coordination bond. The same holds true for structures in which *meta*- and *para*-carbon atoms of a pyridine moiety are involved in the dimer formation: these would not facilitate metal coordination and we did not observe them. These two findings point toward an important role of metal coordination in the covalent bond formation. Figure 6 summarizes the possible dimer structures and their occurrences in the experiment. Although Di3 and Di4 were not observed at all as single entities in our study, reconsidering the tetramer Te1, one realizes that Te1 consists of two such Di3 dimers, which are linked via metal coordination bonds. Similarly, Di3 and Di4 dimers were observed as building blocks of larger clusters Tr2 and Te2, respectively (Figure 7). Interestingly, the highly symmetric Tr1 was formed based on a strict regioselectivity of the pyrazine groups of three neighboring **pap** molecules for dehydrogenation leading to the formation of a hexaazatriphenyl core. It constitutes due to its 3-fold symmetry and its N^N chelating property an established building block for a variety of applications.[20] Alternatively, Tr1 can be described as a three-star version of dipyrido[2,3-*a*:3′,2′-*c*]phenazine, a bridging ligand applied in coordination chemistry.[36]

Figure 7 shows an overview of the most probable structures that were observed and also are the basis for the statistical analysis for regioselectivity. In total we observed 203 bonds that

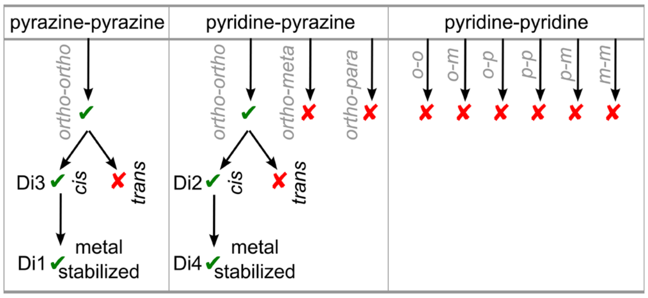

Figure 6. Hierarchy of dimer structures. Dimer structures can be classified according to the bonding moiety (top row), to their bonding positions (second row), relative orientation (third row), and additional metal coordination (bottom row). Structures observed in the experiments are checked, all others crossed, highlighting the strong selectivity of on-surface bond formation. The possibility of metal coordination seems to directly coincide with the respective structure being observed.

have been formed. Among them, 160 bonds occurred between two pyrazine moieties of each two neighboring molecules, 43 between a pyrazine and a pyridine group, and none between two pyridine groups,[37] demonstrating a very strong but not a extremely strict regioselectivity. Note that the latter statistics of the observation of different bond types is made irrespective of whether Au adatoms are involved or not. As each **pap** molecule consists of two pyridine but only one pyrazine moiety, in absence of any regioselectivity one would expect a ratio of occurrences of 1:4:4 of bond-types pyrazine−pyrazine:pyrazine−pyridine:pyridine−pyridine, which is quite opposite to what is observed. When being interpreted in terms of thermodynamic equilibrium at 200 °C and the Boltzmann statistics, the observed occurrences would yield an energy difference of $\Delta E \simeq 2.6$ kcal/mol of pyrazine−pyrazine versus pyrazine−pyridine bonding geometry.

We would like to mention, that some of the images show apparent bonds between neighboring nitrogen atoms. However, such features have been observed before and were identified as imaging artifacts.[34,38] In this context it is important to note that the structural information deduced from the AFM images allows to unambiguously identify which moieties can be involved in the bonds from the molecules' orientations and the distances between heterocycles as presented above irrespective of where exactly real or apparent bonds are observed.

Although a thorough analysis of the mechanism behind our observations goes beyond the scope of this work, we now turn to a brief discussion of a *possible* mechanism behind one aspect of selective bond formation. As mentioned in the context of Figures 5 and 6, only *cis*-N^N-structures bonded in *ortho*−*ortho* geometry enable the incorporation of a gold atom, whereas *meta*-*ortho*-bonded *cis*-N^N-structures as well as all *trans*-N^N-structures do not. Hence, apparently exactly those structures are experimentally observed, which could potentially be stabilized by a coordinating gold atom. Such a gold atom may modify the reactivity of its direct neighborhood, facilitating dehydrogenation. More likely it appears to us, however, that it is rather the geometry that is important: a gold adatom between two monomers, will stabilize two hydrogens each belonging to a different monomer in close proximity, in which a concerted dehydrogenation and immediate bond formation may be facilitated. At the elevated temperature, the entire surface will be subject to constant change and rearrangement, but the presence of coordinating gold adatoms may favor certain geometries over others. When considering such a scenario, the importance of the molecular degrees of freedom being reduced to two dimensions in on-surface chemistry becomes apparent. Note that the regioselectivety concerning the preference for pyrazine-bonded structures observed for the ratio of occurences of different dimers cannot be accounted for by the above considerations alone. Hence, this is a separate aspect of our observations and must stem from a different reactivity of different sites. Thorough theoretical studies on the mechanism and the exact role of Au in these aryl−aryl couplings are ongoing in our laboratory.

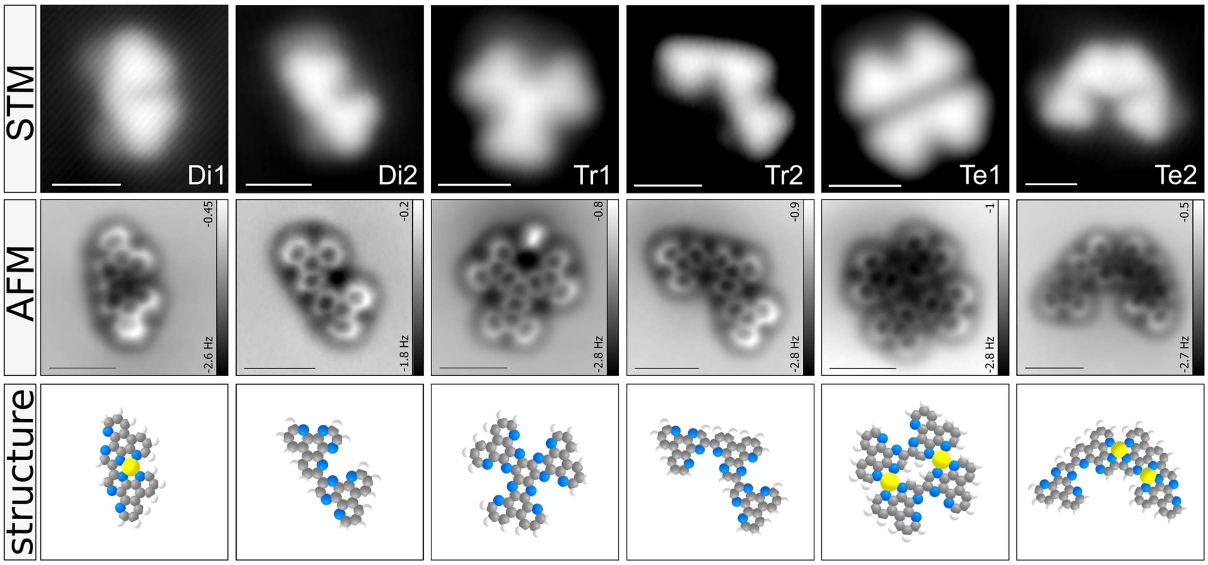

Figure 7. Analysis of main structures observed after covalent bond formation. STM images (top row), AFM images (middle row), and structures (bottom row) for products of dehydrogenation. The structural assignment follows the considerations discussed above.

DOI: 10.1021/jacs.5b13461
J. Am. Chem. Soc. 2016, 138, 5585−5593

■ CONCLUSION

We have demonstrated that pyrazino[2,3-*f*][4,7]-phenanthroline (**pap**) can bond-selectively be transformed through aryl−aryl coupling on an Au(111) surface in UHV conditions into a variety of heterocyclic compounds. The observed regioselectivity of the reactions originates from the fact that *ortho*-hydrogen atoms of the pyrazine rings are preferentially activated for a dehydrogenative C−C bond formation over their pyridine equivalents. Most importantly, the combined STM/AFM study allows a full atomistic analysis of the different reaction products while unambiguously discriminating pyrazine from pyridine moieties. This synthetic strategy to utilize tailored polycyclic precursor molecules comprising pyrazine units will open an avenue for the construction of novel heterocyclic molecules. Depending on the number of pyrazine units incorporated into the starting molecule, the realization of more extended heteroaromatic structures with atomically precise nitrogen locations can be expected.

■ AUTHOR INFORMATION

Corresponding Authors

*nemanja.kocic@ur.de
*liu@dcb.unibe.ch

Notes

The authors declare no competing financial interest.

■ ACKNOWLEDGMENTS

Authors thank Martin Švec and Prokop Hapala for discussions. Financial support from the DFG and GAČR (through RTG1570 and the German-Czech bilateral project RE2669/4−14-16963J), the Volkswagen Foundation through its Lichtenberg program, the Swiss National Science Foundation (Grant No. 200021-147143) and the European Commission (EC) FP7 ITN MOLESCO (Project No. 606728), are gratefully acknowledged.

■ REFERENCES

(1) Bolm, C. *Org. Lett.* **2012**, *14*, 2925.

(2) Rempala, P.; Kroulík, J.; King, B. T. *J. Org. Chem.* **2006**, *71*, 5067.

(3) (a) Li, J. J. *Name Reactions: A Collection of Detailed Reaction Mechanism*, 2nd ed.; Springer-Verlag: New York, 2003. (b) Balaban, A. T.; Nenitzescu, C. D. *Dehydrogenating Condensations of Aromatics (Scholl and Related Reactions)*; Olah, G., Ed.; Wiley: New York, 1964; Vol. 2; pp 979−1047. (c) King, B. T.; Kroulík, J.; Robertson, C. R.; Rempala, P.; Hilton, C. L.; Korinek, J. D.; Gortari, L. M. *J. Org. Chem.* **2007**, *72*, 2279.

(4) (a) Simpson, C. D.; Brand, J. D.; Berresheim, A. J.; Przybilla, L.; Räder, H. J.; Müllen, K. *Chem. - Eur. J.* **2002**, *8*, 1424. (b) Simpson, C. D.; Mattersteig, G.; Martin, K.; Gherghel, L.; Bauer, R. E.; Räder, H. J.; Müllen, K. *J. Am. Chem. Soc.* **2004**, *126*, 3139. (c) Wu, J.; Pisula, W.; Müllen, K. *Chem. Rev.* **2007**, *107*, 718. (d) Narita, A.; Wang, X.-Y.; Feng, X.; Müllen, K. *Chem. Soc. Rev.* **2015**, *44*, 6616.

(5) Grzybowski, M.; Skonieczny, K.; Butenschön, H.; Gryko, D. T. *Angew. Chem., Int. Ed.* **2013**, *52*, 9900.

(6) (a) Gregg, D. J.; Bothe, E.; Höfer, P.; Passaniti, P.; Draper, S. M. *Inorg. Chem.* **2005**, *44*, 5654. (b) Wijesinghe, L. P.; Lankage, B. S.; Máille, G. M. Ó; Perera, S. D.; Nolan, D.; Wang, L.; Draper, S. M. *Chem. Commun.* **2014**, *50*, 10637. (c) Vo, T. H.; Shekhirev, M.; Kunkel, D. A.; Orange, F.; Guinel, M. J.-F.; Enders, A.; Sinitskii, A. *Chem. Commun.* **2014**, *50*, 4172.

(7) (a) Méndez, J.; López, M. F.; Martín-Gago, J. A. *Chem. Soc. Rev.* **2011**, *40*, 4578. (b) Franc, G.; Gourdon, A. *Phys. Chem. Chem. Phys.* **2011**, *13*, 14283. (c) El Garah, M.; MacLeod, J. M.; Rosei, F. *Surf. Sci.* **2013**, *613*, 6. (d) Wiengarten, A.; Seufert, K.; Auwärter, W.; Écija, D.; Diller, K.; Allegretti, F.; Bischoff, F.; Fischer, S.; Duncan, D. A.; Papageorgiou, A. C.; Klappenberger, F.; Acres, R. G.; Ngo, T. H.; Barth, J. V. *J. Am. Chem. Soc.* **2014**, *136*, 9346. (e) Sun, Q.; Zhang, C.; Cai, L.; Xie, L.; Tan, Q.; Xu, W. *Chem. Commun.* **2015**, *51*, 2836. (f) Dong, L.; Liu, P. N.; Lin, N. *Acc. Chem. Res.* **2015**, *48*, 2765. (g) Fan, Q.; Gottfried, J. M.; Zhu, J. *Acc. Chem. Res.* **2015**, *48*, 2484.

(8) Cai, J.; Ruffieux, P.; Jaafar, R.; Bieri, M.; Braun, T.; Blankenburg, S.; Muoth, M.; Seitsonen, A. P.; Saleh, M.; Feng, X.; Müllen, K.; Fasel, R. *Nature* **2010**, *466*, 470.

(9) (a) Blankenburg, S.; Cai, J.; Ruffieux, P.; Jaafar, R.; Passerone, D.; Feng, X.; Müllen, K.; Fasel, R.; Pignedoli, C. A. *ACS Nano* **2012**, *6*, 2020. (b) Huang, H.; Wei, D.; Sun, J.; Wong, S. L.; Feng, Y. P.; Neto, A. C.; Wee, A. T. S. *Sci. Rep.* **2012**, *2*, 983. (c) Dienel, T.; Kawai, S.; Söde, H.; Feng, X.; Müllen, K.; Ruffieux, P.; Fasel, R.; Gröning, O. *Nano Lett.* **2015**, *15*, 5185. (d) Chen, Y.-C.; Cao, T.; Chen, C.; Pedramrazi, Z.; Haberer, D.; de Oteyza, D. G.; Fischer, F. R.; Louie, S. G.; Crommie, M. F. *Nat. Nanotechnol.* **2015**, *10*, 156. (e) Liu, J.; Li, B.-W.; Tan, Y.; Giannakopoulos, A.; Sanchez-Sanchez, C.; Beljonne, D.; Ruffieux, P.; Fasel, R.; Feng, X.; Müllen, K. *J. Am. Chem. Soc.* **2015**, *137*, 6097.

(10) (a) Pinardi, A. L.; Otero-Irurueta, G.; Palacio, I.; Martinez, J. I.; Sanchez-Sanchez, C.; Tello, M.; Rogero, C.; Cossaro, A.; Preobrajenski, A.; Gómez-Lor, B. *ACS Nano* **2013**, *7*, 3676. (b) Pinardi, A. L.; Martínez, J. I.; Jančařík, A.; Stará, I. G.; Starý, I.; López, M. F.; Méndez, J.; Martín-Gago, J. Á. *Chem. Commun.* **2014**, *50*, 1555. (c) Liang, L.; Meunier, V. *J. Phys. Chem. C* **2015**, *119*, 775.

(11) Dienel, T.; Gómez-Díaz, J.; Seitsonen, A. P.; Widmer, R.; Iannuzzi, M.; Radican, K.; Sachdev, H.; Müllen, K.; Hutter, J.; Gröning, O. *ACS Nano* **2014**, *8*, 6571.

(12) (a) Usachov, D.; Vilkov, O.; Grüneis, A.; Haberer, D.; Fedorov, A.; Adamchuk, V. K.; Preobrajenski, A. B.; Dudin, P.; Barinov, A.; Oehzelt, M.; Laubschat, C.; Vyalikh, D. V. *Nano Lett.* **2011**, *11*, 5401. (b) Bronner, C.; Stremlau, S.; Gille, M.; Brauße, F.; Haase, A.; Hecht, S.; Tegeder, P. *Angew. Chem., Int. Ed.* **2013**, *52*, 4422.

(13) (a) Wiengarten, A.; Lloyd, J. A.; Seufert, K.; Reichert, J.; Auwärter, W.; Han, R.; Duncan, D. A.; Allegretti, F.; Fischer, S.; Oh, S. C.; Saglam, O.; Jiang, L.; Vijayaraghavan, S.; Écija, D.; Papageorgiou, A. C.; Barth, J. V. *Chem. - Eur. J.* **2015**, *21*, 12285. (b) Somorjai, G. A.; Park, J. Y. *Angew. Chem., Int. Ed.* **2008**, *47*, 9212. (c) Sun, Q.; Zhang, C.; Kong, H.; Tan, Q.; Xu, W. *Chem. Commun.* **2014**, *50*, 11825.

(14) Gottfried, J. M. *Surf. Sci. Rep.* **2015**, *70*, 259.

(15) Lafferentz, L.; Eberhardt, V.; Dri, C.; Africh, C.; Comelli, G.; Esch, F.; Hecht, S.; Grill, L. *Nat. Chem.* **2012**, *4*, 215.

(16) Björk, J.; Stafström, S.; Hanke, F. *J. Am. Chem. Soc.* **2011**, *133*, 14884.

(17) Gross, L.; Mohn, F.; Moll, N.; Liljeroth, P.; Meyer, G. *Science* **2009**, *325*, 1110.

(18) (a) Gross, L.; Mohn, F.; Moll, N.; Meyer, G.; Ebel, R.; Abdel-Mageed, W. M.; Jaspars, M. *Nat. Chem.* **2010**, *2*, 821. (b) Pavliček, N.; Fleury, B.; Neu, M.; Niedenführ, J.; Herranz-Lancho, C.; Ruben, M.; Repp, J. *Phys. Rev. Lett.* **2012**, *108*, 086101. (c) Hanssen, K. Ø.; Schuler, B.; Williams, A. J.; Demissie, T. B.; Hansen, E.; Andersen, J. H.; Svenson, J.; Blinov, K.; Repisky, M.; Mohn, F.; Meyer, G.; Svendsen, J.-S.; Ruud, K.; Elyashber, M.; Gross, L.; Jaspars, M.; Isaksson, J. *Angew. Chem., Int. Ed.* **2012**, *124*, 12238. (d) Schuler, B.; Liu, S.-X.; Geng, Y.; Decurtins, S.; Meyer, G.; Gross, L. *Nano Lett.* **2014**, *14*, 3342.

(19) (a) Albrecht, F.; Neu, M.; Quest, C.; Swart, I.; Repp, J. *J. Am. Chem. Soc.* **2013**, *135*, 9200. (b) Albrecht, F.; Pavliček, N.; Herranz-Lancho, C.; Ruben, M.; Repp, J. *J. Am. Chem. Soc.* **2015**, *137*, 7424. (c) Mohn, F.; Repp, J.; Gross, L.; Meyer, G.; Dyer, M. S.; Persson, M. *Phys. Rev. Lett.* **2010**, *105*, 266102. (d) Riss, A.; Wickenburg, S.; Gorman, P.; Tan, L. Z.; Tsai, H.-Z.; de Oteyza, D. G.; Chen, Y.-C.; Bradley, A. J.; Ugeda, M. M.; Etkin, G.; Louie, S. G.; Fischer, F. R.; Crommie, M. F. *Nano Lett.* **2014**, *14*, 2251. (e) Hla, S.-W.; Bartels, L.; Meyer, G.; Rieder, K.-H. *Phys. Rev. Lett.* **2000**, *85*, 2777. (f) de Oteyza, D. G.; Gorman, P.; Chen, Y.-C.; Wickenburg, S.; Riss, A.; Mowbray, D.

J.; Etkin, G.; Pedramrazi, Z.; Tsai, H.-Z.; Rubio, A.; Crommie, M. F. *Science* **2013**, *340*, 1434.

(20) (a) Bergkamp, J.; Decurtins, S.; Liu, S.-X. *Chem. Soc. Rev.* **2015**, *44*, 863. (b) Liu, B.; Ran, Y.-F.; Li, Z.; Liu, S.-X.; Jia, C.; Decurtins, S.; Wandlowski, T. *Chem. - Eur. J.* **2010**, *16*, 5008. (c) Jia, C.; Liu, S.-X.; Tanner, C.; Leiggener, C.; Sanguinet, L.; Levillain, E.; Leutwyler, S.; Hauser, A.; Decurtins, S. *Chem. Commun.* **2006**, 1878. (d) Wu, J.; Dupont, N.; Liu, S.-X.; Neels, A.; Hauser, A.; Decurtins, S. *Chem. - Asian J.* **2009**, *4*, 392.

(21) Kocić, N.; Weiderer, P.; Keller, S.; Decurtins, S.; Liu, S.-X.; Repp, J. *Nano Lett.* **2015**, *15*, 4406.

(22) Abeywickrama, C.; Baker, A. D. *J. Org. Chem.* **2004**, *69*, 7741.

(23) (a) Fuchs, Y.; Lofters, S.; Dieter, T.; Shi, W.; Morgan, R.; Strekas, T. C.; Gafney, H. D.; Baker, A. D. *J. Am. Chem. Soc.* **1987**, *109*, 2691. (b) Grove, H.; Sletten, J.; Julve, M.; Lloret, F.; Cano, J. *J. Chem. Soc., Dalton Trans.* **2001**, 259. (c) Grove, H.; Sletten, J. *J. Chem. Crystallogr.* **2000**, *30*, 123. (d) González, I.; Dreyse, P.; Cortés-Arriagada, D.; Sundararajan, M.; Morgado, C.; Brito, I.; Roldán-Carmona, C.; Bolink, H. J.; Loeb, B. *Dalton Trans.* **2015**, *44*, 14771.

(24) Giessibl, F. J. *Appl. Phys. Lett.* **2000**, *76*, 1470.

(25) Soler, J. M.; Artacho, E.; Gale, J. D.; García, A.; Junquera, J.; Ordejón, P.; Sánchez-Portal, D. *J. Phys.: Condens. Matter* **2002**, *14*, 2745.

(26) Blum, V.; Gehrke, R.; Hanke, F.; Havu, P.; Havu, V.; Ren, X.; Reuter, K.; Scheffler, M. *Comput. Phys. Commun.* **2009**, *180*, 2175.

(27) Tkatchenko, A.; Scheffler, M. *Phys. Rev. Lett.* **2009**, *102*, 073005.

(28) Hapala, P.; Kichin, G.; Wagner, C.; Tautz, F. S.; Temirov, R.; Jelínek, P. *Phys. Rev. B: Condens. Matter Mater. Phys.* **2014**, *90*, 085421.

(29) Hapala, P.; Temirov, R.; Tautz, F. S.; Jelínek, P. *Phys. Rev. Lett.* **2014**, *113*, 226101.

(30) Giessibl, F. J. *Appl. Phys. Lett.* **2001**, *78*, 123.

(31) Kawai, S.; Saito, S.; Osumi, S.; Yamaguchi, S.; Foster, A. S.; Spijker, P.; Meyer, E. *Nat. Commun.* **2015**, *6*, 8098.

(32) (a) Neu, M.; Moll, N.; Gross, L.; Meyer, G.; Giessibl, F. J.; Repp, J. *Phys. Rev. B: Condens. Matter Mater. Phys.* **2014**, *89*, 205407. (b) Moll, N.; Schuler, B.; Kawai, S.; Xu, F.; Peng, L.; Orita, A.; Otera, J.; Curioni, A.; Neu, M.; Repp, J. *Nano Lett.* **2014**, *14*, 6127.

(33) (a) Shi, Z.; Lin, N. *J. Am. Chem. Soc.* **2009**, *131*, 5376. (b) Maksymovych, P.; Sorescu, D. C.; Yates, J. T., Jr *Phys. Rev. Lett.* **2006**, *97*, 146103. (c) Stepanow, S.; Lin, N.; Payer, D.; Schlickum, U.; Klappenberger, F.; Zoppellaro, G.; Ruben, M.; Brune, H.; Barth, J. V.; Kern, K. *Angew. Chem.* **2007**, *119*, 724. (d) Pawin, G.; Wong, K. L.; Kim, D.; Sun, D.; Bartels, L.; Hong, S.; Rahman, T. S.; Carp, R.; Marsella, M. *Angew. Chem., Int. Ed.* **2008**, *47*, 8442. (e) Mielke, J.; Hanke, F.; Peters, M. V.; Hecht, S.; Persson, M.; Grill, L. *J. Am. Chem. Soc.* **2015**, *137*, 1844. (f) Yang, Z.; Corso, M.; Robles, R.; Lotze, C.; Fitzner, R.; Mena-Osteritz, E.; Bäuerle, P.; Franke, K. J.; Pascual, J. I. *ACS Nano* **2014**, *8*, 10715.

(34) Hämäläinen, S. K.; van der Heijden, N.; van der Lit, J.; den Hartog, S.; Liljeroth, P.; Swart, I. *Phys. Rev. Lett.* **2014**, *113*, 186102.

(35) van der Lit, J.; Di Cicco, F.; Prokop, H.; Jelínek, P.; Swart, I. *Phys. Rev. Lett.* **2016**, *116*, 0961012.

(36) Ran, Y.-F.; Liu, S.-X.; Sereda, O.; Neels, A.; Decurtins, S. *Dalton Trans.* **2011**, *40*, 8193.

(37) There are a few observations of bonds that could not be unambiguously identified. We therefore provide an upper limit of at most 2% of pyridine−pyridine bonded structures.

(38) (a) Sweetman, A.; Jarvis, S.; Sang, H.; Lekkas, I.; Rahe, P.; Wang, Y.; Wang, J.; Champness, N.; Kantorovich, L.; Moriarty, P. *Nat. Commun.* **2014**, *5*, 3931. (b) Pavliček, N.; Herranz-Lancho, C.; Fleury, B.; Neu, M.; Niedenführ, J.; Ruben, M.; Repp, J. *Phys. Status Solidi B* **2013**, *250*, 2424.

nature chemistry

ARTICLES

PUBLISHED ONLINE: 21 NOVEMBER 2016 | DOI: 10.1038/NCHEM.2662

From helical to planar chirality by on-surface chemistry

Oleksandr Stetsovych[1], Martin Švec[1], Jaroslav Vacek[2], Jana Vacek Chocholoušová[2], Andrej Jančařík[2], Jiří Rybáček[2], Krzysztof Kosmider[1], Irena G. Stará[2], Pavel Jelínek[1]* and Ivo Starý[2]*

The chirality of molecular structures is paramount in many phenomena, including enantioselective reactions, molecular self-assembly, biological processes and light or electron-spin polarization. Flat prochiral molecules, which are achiral in the gas phase or solution, can exhibit adsorption-induced chirality when deposited on surfaces. The whole array of such molecular adsorbates is naturally racemic as spontaneous global mirror-symmetry breaking is disfavoured. Here we demonstrate a chemical method of obtaining flat prochiral molecules adsorbed on the solid achiral surface in such a way that a specific adsorbate handedness globally dominates. An optically pure helical precursor is flattened in a cascade of on-surface reactions, which enables chirality transfer. The individual reaction products are identified by high-resolution scanning-probe microscopy. The ultimate formation of globally non-racemic assemblies of flat molecules through stereocontrolled on-surface synthesis allows for chirality to be expressed in as yet unexplored types of organic–inorganic chiral interfaces.

Chirality (a geometric property of any object that is not superimposable on its mirror image) is inherent in nature, as manifested by the existence of homochiral proteins, nucleic acids and polysaccharides that express stereospecific interactions in various molecular events[1]. An efficient control over the relative or absolute stereochemistry in organic reactions is one of the greatest achievements of in-solution chemistry within the past half-century[2].

A new opportunity to tackle the problem of induction and transformation of single-molecule chirality in on-surface reactions monitored at the nanoscale has emerged with the recent progress in scanning-probe microscopy (SPM) techniques, and has made possible the acquisition of high-resolution images of molecules on surfaces with submolecular resolution[3–6]. This achievement indicates a potential to pursue not only the structural analysis and property investigation of individual organic molecules, but also chemical synthesis at the nanoscopic scale[7–9]. Indeed, complex chemical transformations of single molecules are currently traced by high-resolution scanning tunnelling microscopy (STM) along with non-contact atomic force microscopy (nc-AFM)[10,11]. Evidently, these methods have matured enough to focus on intriguing aspects of single-molecule chirality.

The first successful steps that described stereoinduction in chemisorbed chiral modifier–prochiral substrate complexes important for enantioselective heterogeneous hydrogenation have recently been made using submolecular-resolution STM[12]. To date, however, in the context of molecular chirality monitored at the nanoscale[13], significant attention has been paid only to the adsorption and organization of intrinsically chiral or prochiral molecules on achiral or chiral surfaces[14,15]. In the case of racemic or achiral molecules that form chiral adsorbates, local mirror-symmetry breaking in their assemblies may occur. It happens locally if two-dimensional (2D) conglomerates[16,17], homochiral clusters[18,19] or mirror domain structures[20] are spontaneously formed. However, globally there is no observable imbalance between the populations of enantiomeric entities. However, such a stochastic behaviour may be overwhelmed by a chiral bias applied through, for example, the nonlinear amplification of enantiomeric imbalance[21,22], co-adsorption of a homochiral auxiliary[23] or the influence of a homochiral solvent[24].

On the other hand, flat molecules endowed only with mirror symmetry with respect to the plane of their backbone are achiral. On adsorption on a solid surface, however, they form chiral adsorbates as they are also prochiral. This relates to the phenomenon of planar chirality that exists at non-symmetrically substituted transition-metal arene π complexes[25], ferrocenes[26] or cyclophanes[27]. Importantly, spontaneous global mirror-symmetry breaking in the 2D assemblies of the flat prochiral molecules is very unlikely (Fig. 1, path B) as both their faces interact equally with the achiral surface to form a globally racemic system (Fig. 1, path C).

Here we show the possibility to reach indirectly the enantiofacial adsorption of flat prochiral molecules on an achiral metal surface to afford highly enantioenriched adsorbates. Such a global mirror-symmetry breaking in the system of prochiral molecules is possible owing to the chirality transfer from the homochiral helical precursor to the enantiofacially adsorbed prochiral molecules through a cascade of on-surface transformations (Fig. 1, path A, and on-surface reaction at T_1).

Results and discussion

To demonstrate the envisioned on-surface chirality transfer, we focused on the helically chiral benzo[2,1-*g*:3,4-*g*′]dichrysene (dibenzo[*i*,*o*]heptahelicene (**DBH**))[28] (inset in Fig. 2a) that exists in the two enantiomeric *M* and *P* forms. There were two main reasons to choose this model compound specifically: (1) it has a reasonably high barrier to thermal racemization of 40.9 kcal mol^{-1} (1.77 eV, measured at 503 K in hexadecane[28]) that allows it to be handled at elevated temperatures without the risk of losing enantiopurity significantly (the half-life of enantiopure **DBH** ($t_{1/2}$) in hexadecane was calculated to be 5.5 hours at 503 K) and (2) on-surface transformation of the 3D **DBH** is expected to be driven to planarization to release the internal torsional strain. We have already described the planarization of a 3D helicene molecule on annealing on various metals, but the question of the chirality transfer was not addressed[29,30].

---

[1]Institute of Physics, Czech Academy of Sciences, Cukrovarnická 10, 162 00 Prague 6, Czech Republic. [2]Institute of Organic Chemistry and Biochemistry, Czech Academy of Sciences, Flemingovo nám. 2, 166 10 Prague 6, Czech Republic. *e-mail: jelinekp@fzu.cz; stary@uochb.cas.cz

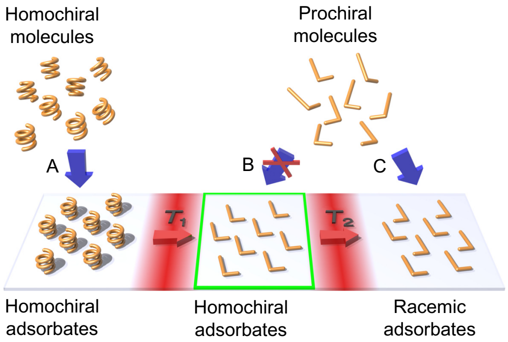

Figure 1 | Proposed concept of global mirror-symmetry breaking in the system of prochiral molecules on an achiral substrate. In path A, the vacuum deposition of homochiral molecules (represented here by helices of the same handedness) onto an achiral substrate provides homochiral adsorbates. For path B, the vacuum deposition of prochiral molecules (represented here by L-shaped objects) onto an achiral substrate does not lead to homochiral (or enantioenriched) adsorbates as spontaneous global mirror-symmetry breaking is disfavoured. In path C, vacuum deposition of prochiral molecules onto an achiral substrate delivers racemic adsorbates. At temperature T_1 an on-surface transformation of homochiral molecules into enantiofacially adsorbed prochiral molecules occurs to form homochiral (or enantioenriched) adsorbates (adsorption-induced chirality is controlled by the chirality transfer and results in global mirror-symmetry breaking). At temperature T_2 ($>T_1$) on-surface racemization (scrambling of enantiofacial adsorption) of the originally homochiral (or enantioenriched) adsorbates takes place and the transferred chirality is lost.

To start with, we deposited, by high-vacuum sublimation, the enantiopure (*P*)-**DBH** onto an Ag(111) surface with a molecular concentration of ~11.4 ± 0.4 molecules per 10×10 nm^2. STM imaging revealed the formation of homochiral trimers that appeared as equilateral triangles (95% of the molecules (Fig. 2a); Supplementary Fig. 1 gives the detailed statistics). Most of them had the same azimuthal orientation (94%), but some were rotated by 90° (6%). In contrast, the racemic *rac*-**DBH** preferred apparently heterochiral dimers (98% at a molecular concentration of ~11.1 ± 0.4 molecules per 10×10 nm^2) randomly rotated by 60° with respect to each other (Supplementary Fig. 2). Although certain similarities in the growth behaviour of the parent racemic and enantiopure heptahelicene on metal surfaces have recently been reported[21,31], congeneric *rac*-dibenzo[*f,j*]picene was described to crystallize as a 2D conglomerate[32].

A completely different STM morphology of molecular adsorbates was obtained on annealing the enantiopure (*P*)-**DBH** on Ag(111) at elevated temperatures (neglecting the chirality aspects at this moment, the importance of which will be discussed later, *rac*-**DBH** behaved identically on annealing). The first transition was relatively sharp once the threshold of 520 K was reached. Keeping the adsorbed (*P*)-**DBH** at this temperature for about five minutes, the helicene molecules completely disappeared giving rise to new adsorbates of strikingly different structures (Fig. 2b). At a concentration of ~8.6 ± 0.4 molecules per 10×10 nm^2, dimers (hourglass shaped, 55% of all molecules) and tetramers (four-arm stars, 23%) dominated in the STM images. Trimers were also observed but at a considerably lower concentration (2%). In addition, separate non-symmetrical (13%) and symmetrical (5%) monomers were found as single bright protrusions of the characteristic shape. Supplementary Fig. 3 gives the detailed statistics. All these objects were randomly rotated by 60° with respect to each other. At a higher molecular concentration (~14.5 ± 0.5 molecules per 10×10 nm^2), interestingly, the ratio between the dimers (31% of all the molecules) and tetramers (four-arm stars, 50%) significantly changed in favour of the tetramers (Supplementary Fig. 4 gives the detailed statistics).

Further annealing brought the system to the gradual second transition that was well pronounced at temperatures above 620 K, as imaged by STM. Hence, the follow-up heating of the molecular adsorbates, which originated from (*P*)-**DBH** at the molecular concentration of ~8.6 ± 0.4 molecules per 10×10 nm^2, on Ag(111) at 670 K for five minutes, the four-arm star tetramers completely disappeared and the number of dimers dramatically decreased (only ~7.5% of all molecules were incorporated in them (Fig. 2c)). Instead, the separate non-symmetrical monomers observed as single bright protrusions of the characteristic shape dominated (~84%). The separate symmetrical monomers (~7.5%) were also observed, but their number was comparable to that found after annealing at 520 K. Only a few molecules (~1%) were encountered that were difficult to identify (Supplementary Fig. 5 gives the detailed statistics).

To explain the thermally induced stepwise changes in the morphology of the molecular adsorbates, we attempted a structural identification of the reaction products. STM-tip manipulation with the components of the tetramers (Supplementary Fig. 6) demonstrated that they are, in fact, linked by non-covalent bonds. The simultaneous STM and nc-AFM imaging further revealed that the triangular parts of the dimers (Fig. 3d,h) or tetramers (Fig. 3e,i) are flat. However, the two small bulges (bright lobes) in the middle of the dimers or the four bulges located in the centre of the tetramers protrude from the surface as indicated by the corresponding repulsion in the nc-AFM channel. The protruding parts of these clusters ultimately hindered a further decrease in the tip–sample distance necessary to obtain intramolecular resolution. Thus, based on a theoretical and reaction-mechanism analysis (see below) we assigned the structure of 6-phenyldibenzo[*a,g*]coronene (**P1**) (Fig. 3a) to the monomeric components of the dominant dimers (hourglass shaped), rare trimers and minor tetramers (four-arm stars). We used a density functional theory (DFT) method to optimize the structure of the dimer as well as the tetramer composed from the corresponding number of molecules **P1** enantiofacially adsorbed on Ag(111) (Fig. 3l,m). The calculation outputs confirmed that the stability of the proposed molecular clusters benefitted from multiple intermolecular CH–π interactions between the out-of-the-plane twisted phenyl ring and a proximal hydrogen atom of the adjacent molecule. The corresponding calculated nc-AFM images of the optimized molecular structures are in good agreement with the experimental ones (Supplementary Fig. 7). In contrast, the flat structure of the monomer products allowed the acquisition of high-resolution nc-AFM imaging with intramolecular details (Fig. 3j,k). Accordingly, the symmetrical and non-symmetrical monomers were identified unambiguously as dibenzo[*a,m*]indeno[1,2,3-*e,f*]coronene (**P2**) (Fig. 3b) and dibenzo[*a,g*]coronene (**P3**) (Fig. 3c), respectively. Furthermore, the measured high-resolution contrasts for the **P1**, **P2** and **P3** products are in excellent agreement with the AFM simulator (Supplementary Fig. 7).

To outline the reaction mechanism of the thermally induced on-surface transformation of the initial (*P*)-**DBH** to **P1**, **P2** and **P3**, we propose that the cascade of intramolecular reactions is initiated at 520 K by Diels–Alder [4+2] cycloaddition that converts (*P*)-**DBH** to intermediate **A** (Fig. 3p). The subsequent dehydrogenation step results in intermediate **B**, which represents a bifurcation point of the mechanism: Either benzyne can be extruded (by a retro Diels–Alder cycloaddition) to furnish the symmetrical coronene derivative **P3** as a side product or, predominantly, a C–C bond rupture in the bridged tricyclic subunit takes place (at the quaternary sp^3 carbon atom) coupled with a hydrogen shift. This yields the non-symmetrical phenyl-substituted coronene derivative **P1** as the main product. Then, at a higher temperature (670 K), cyclodehydrogenation of **P1** is completed to yield the final flat non-symmetric coronene derivative **P2**. There are circumstantial pieces of evidence in favour of an initial Diels–Alder cycloaddition: (1) an aryne cycloaddition within the helicene skeleton has been described already[33], (2) on electron-impact ionization (EI) in mass spectrometry (MS), (hetero)helicenes tend to

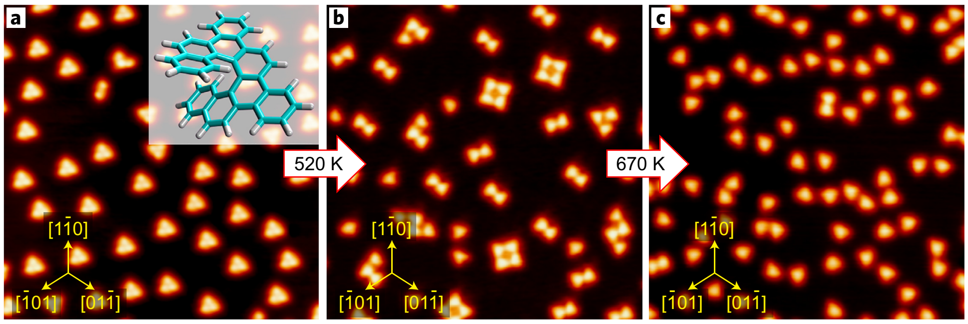

Figure 2 | The enantiopure benzo[2,1-*g*:3,4-*g*′]dichrysene (*P*)-DBH on Ag(111) and changes in morphology of adsorbates on annealing at 520 and 670 K. STM overview images at 1.2 K, $I_t = 20$ pA and $U = 500$ mV, with a molecular concentration of ~11.4 ± 0.4 molecules per 10 × 10 nm^2 and of size 30 × 30 nm^2. **a**, (*P*)-DBH before annealing. **b**, (*P*)-DBH after annealing at 520 K for 5 min. **c**, (*P*)-DBH after annealing at 670 K for 5 min. The inset in **a** shows a model of the (*P*)-DBH enantiomer ($C_{38}H_{22}$).

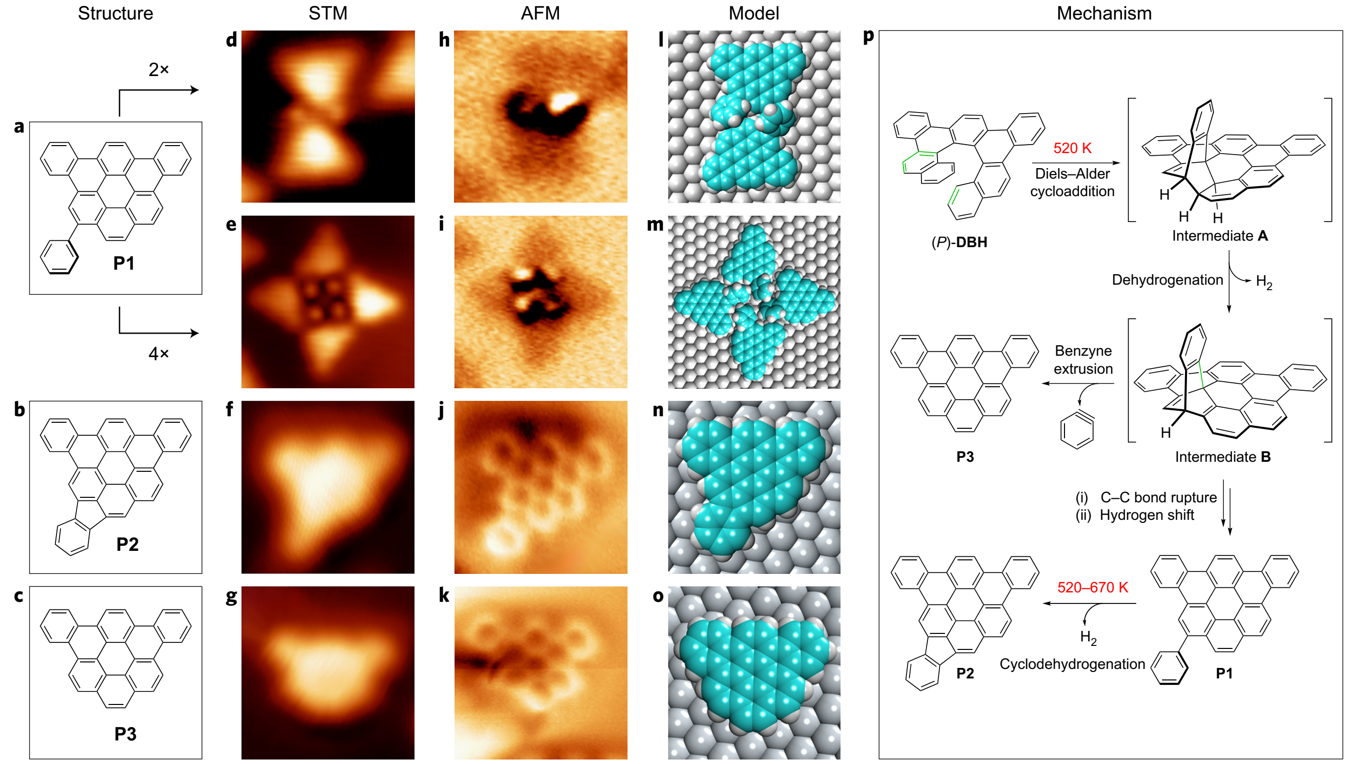

Figure 3 | Transformation products P1, P2 and P3 of the annealing of (*P*)-DBH on Ag(111) at 520–670 K, and elucidation of their structures, calculated models and proposed reaction mechanism. a–o, The chemical structure of the transformation products P1 (**a**), P2 (**b**) and P3 (**c**). Constant-height STM images taken at 1.2 K, $U = 3$ mV (**d**,**e**), 1 mV (**f**) or 0.5 mV (**g**). Simultaneously recorded nc-AFM images taken with the Xe-functionalized tip (**h**–**k**), and optimized structures of molecular adsorbates obtained from the DFT calculations (**l**–**o**). STM and corresponding AFM images of the dimer of P1, size 3 × 3 nm^2 (**d**,**h**). STM and corresponding AFM images of the four-arm star tetramer of P1, size 4.4 × 4.4 nm^2 (**e**,**i**). STM and corresponding AFM images of the monomeric P2, size 2 × 2 nm^2 (**f**,**j**). STM and corresponding AFM images of the monomeric P3, size 2 × 2 nm^2 (**g**,**k**). **p**, Proposed mechanism of the cascade transformations of (*P*)-DBH to the coronene derivatives P1, P2 and P3 on annealing on Ag(111) at 520 and 670 K. The multiple bonds in (*P*)-DBH marked in green represent the diene and dienophile systems involved in the following Diels–Alder cycloaddition; the single bond in the intermediate **B** (marked in green) breaks on the way to product P1.

fragment into coronene ions via Diels–Alder cycloadducts[34] (correspondingly, **DBH** in EI MS shows a fragment of $m/z = 400$ associated with P3) and, most importantly, (3) it has been demonstrated that the parent heptahelicene undergoes in-solution skeletal rearrangements mediated by $AlCl_3$ (ref. 35) or AuCl/Ag[Al(OC(CF_3)$_3$)$_4$] (ref. 36) and initiated by intramolecular Diels–Alder cycloaddition to provide an oxidized coronene derivative or coronene-derived carbocation, respectively (analogous intermediates to **A** and **B** were proposed in these rearrangements). Apparently, the reaction cascade may consist of unimolecular reactions as stable non-covalently bound molecular clusters observed at 1.2 K are not expected to exist at the temperatures of the aforementioned reactions. However, we cannot exclude the influence of neighbouring molecules on the reaction mechanism or minor chirality scrambling, which is now under investigation.

The trajectory of the initial Diels–Alder cycloaddition of (*P*)-**DBH** on Ag(111) was calculated from first principles using the periodic DFT and NEB (nudged elastic band) algorithm to localize the transition state (Supplementary Fig. 8). The synchronous reaction features a barrier of 24.3 kcal mol^{-1} (1.05 eV) that is somewhat underestimated as (*P*)-**DBH** requires heating over 520 K on a timescale of minutes

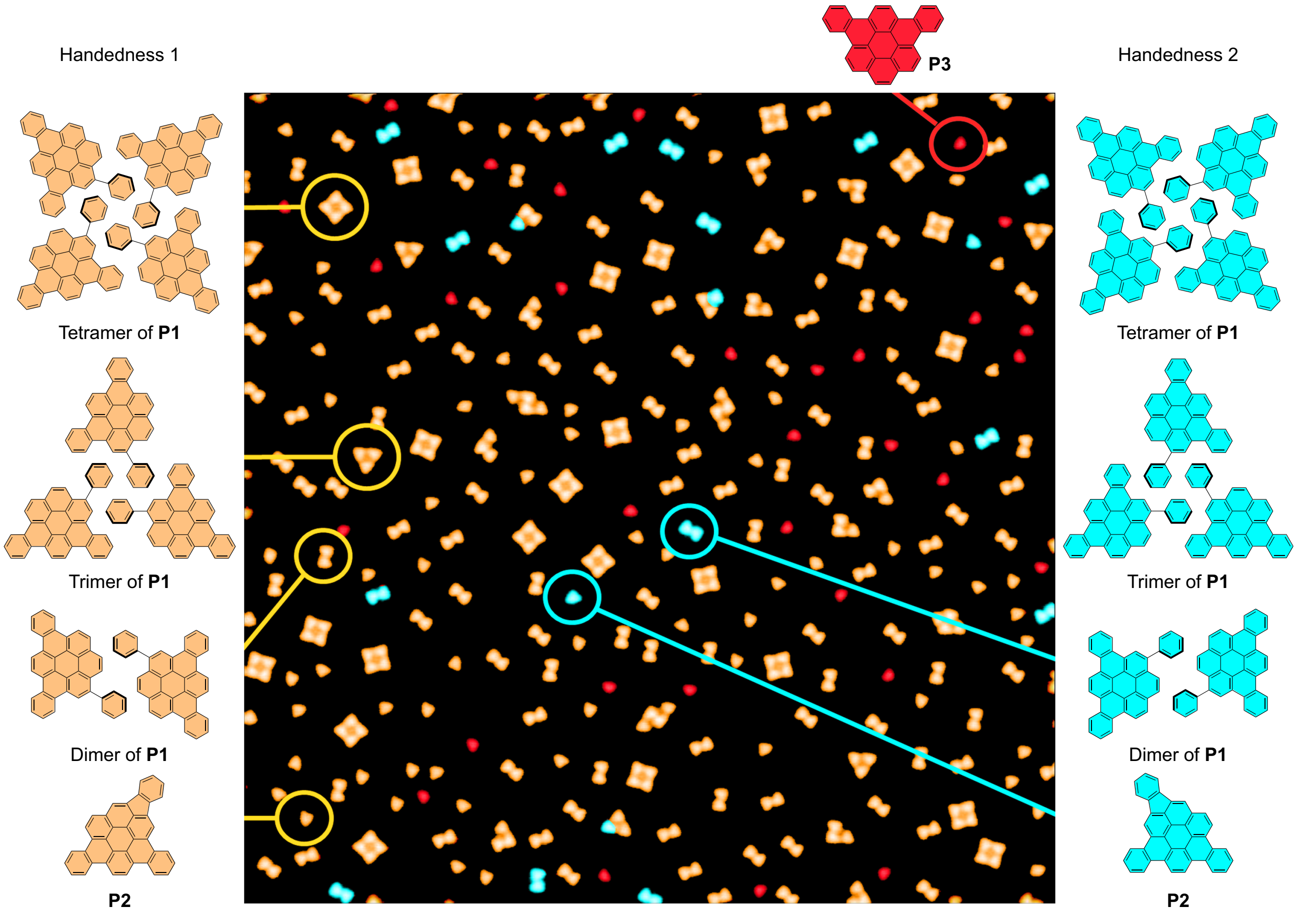

Figure 4 | Distribution of the handednesses of the adsorbed products P1 and P2 after annealing the enantiopure (*P*)-DBH on Ag(111) at 520 K for 5 min. The coloured STM overview image (centre) was taken at 1.2 K, $I_t = 20$ pA and $U = -500$ mV, with a molecular concentration of ~7.9 ± 0.4 molecules per 10 × 10 nm^2, and of size 80 × 80 nm^2. Orange and cyan spots represent the molecular adsorbates **P1** and **P2**, respectively, sorted by their handedness; red spots represent the achiral molecular adsorbates **P3**. The structures of the molecular entities of different handedness found on the surface after the annealing are shown on both sides of the STM image (tetramers and trimers of **P1** possessing handedness 2 are not present in this STM image).

to undergo the cycloaddition and trigger the subsequent cascade transformation. Also, (*P*)-**DBH** does not undergo the Diels–Alder cycloaddition in hexadecane under heating at 503 K over one hour (*vide supra*) as only partial racemization takes place.

Next, we discuss the possibility of the on-surface transformation of homochiral molecules into enantiofacially adsorbed prochiral molecules. In particular, the transformation of the enantiopure reactant (*P*)-**DBH** into the chiral intermediates **A** and **B**, and into the prochiral coronene derivatives **P1** and **P2**, which exist as chiral molecular adsorbates (the molecule **P3** is not prochiral), raises the question of the conservation or scrambling of handedness along the reaction coordinate. Actually, such a challenging problem of the chirality preservation and/or transformation in on-surface reactions of single-molecule adsorbates monitored at the nanoscale, to our knowledge, has not yet been addressed. Owing to the high-resolution STM images and characteristic morphology of the chiral molecular adsorbates **P1** and **P2**, we could enumerate the ratio of their populations of a given handedness (Fig. 4). For this purpose, we analysed manually large scans (80 × 80 nm^2, each of them encompassing over 500 molecules; Supplementary Fig. 9 gives the assignment of the handedness to the adsorbates **P1** in clusters or to the individual adsorbates **P2**).

The statistics over both the occurrence of the chiral molecular adsorbates **P1** and **P2** (**P3** is not chiral) and their handedness after annealing (*P*)-**DBH** on Ag(111) at various temperatures (520–670 K) revealed unprecedented chirality transfer from the enantiopure reactant (*P*)-**DBH** to the enantiofacially adsorbed prochiral molecules **P1** and **P2** (Fig. 5 and Table 1; Supplementary Tables 1–5 give the details). By annealing the sample at 520 K for five minutes, the chiral adsorbates **P1** and **P2** as the main products were significantly enantioenriched. Their e.r. values (handedness 1/handedness 2) were assessed to be 92:8 and 91:9, respectively (Table 1, entry 1). Surprisingly, these e.r. values remained practically unchanged up to 590 K. This indicates a configurational stability of the enantiofacially adsorbed **P1** and **P2** (Table 1, entries 2 and 3). Above this temperature limit, however, noticeable racemization of the chiral adsorbates **P1** and **P2** took place, which resulted finally in the formation of a racemic adlayer at 670 K (Table 1, entries 4 and 5). Hence, an incomplete chirality transfer from the enantiopure (*P*)-**DBH** to the enantiofacially adsorbed **P1** and **P2** at 520 K is not the result of a partial racemization of them at this temperature (see note under Supplementary Fig. 9). In a control experiment, we annealed the enantioenriched (*M*)-**DBH** (*M*:*P* = 93:7) on Ag(111) at 520 K for five minutes and analysed the handedness distribution in the chiral adsorbates **P1** (major) and **P2** (minor, Supplementary Table 6). Their e.r. values (handedness 1/handedness 2) were found to be 18:82 and 13:87, respectively, to reflect the opposite helicity of the precursors (*M*)-**DBH** versus (*P*)-**DBH** (Supplementary Table 1). The formally diminished chirality transfer in the transformation of (*M*)-**DBH** can be explained by its lower optical purity. Thus, the thermal behaviours of the two enantiomers

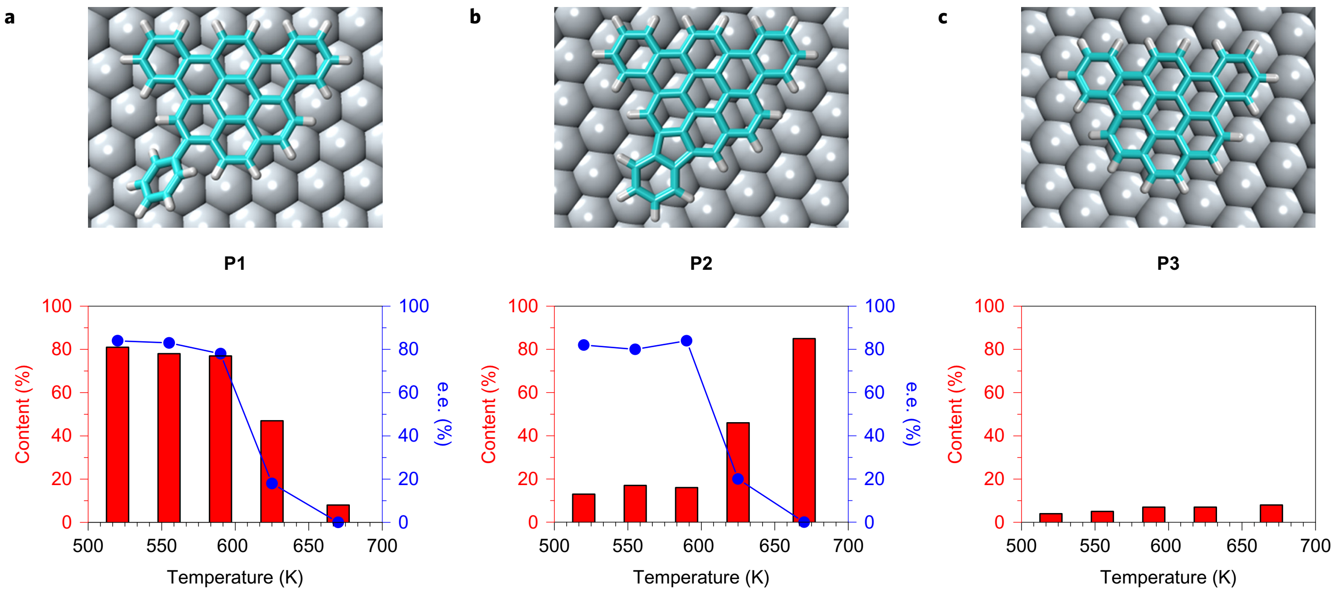

Figure 5 | The occurrence of the molecular adsorbates P1, P2 and P3 and % e.e. of P1 and P2 after annealing the enantiopure (*P*)-DBH on Ag(111) at various temperatures. The statistics are based on the analysis of the STM images (Supplementary Tables 1–5 give the details). The e.r. corresponds to the ratio between the adsorbates that exhibit handedness 1 or 2 (the arbitral assignment of handednesses 1 and 2 to the molecular adsorbates P1 and P2 is shown in Fig. 4). **a–c**, Content (%, red bars) of P1 (composed of various clusters) (**a**), P2 (**b**) and P3 (**c**) as well as the % e.e. (blue lines) of P1 and P2 in the mixtures of adsorbates after annealing the enantiopure (*P*)-DBH at different temperatures for 5 min; % e.e. corresponds to the difference in the fractions that yield the e.r. (Table 1).

Table 1 | Statistics for molecular adsorbates P1, P2 and P3 and for the e.r. of P1 and P2.

Entry	Annealing temperature (K)	Adsorbate P1		Adsorbate P2		Adsorbate P3 (no. of molecules)	Unidentified adsorbates (no. of molecules)
		No. of molecules	e.r. (%)	No. of molecules	e.r. (%)		
1	520	885	92:8	140	91:9	49	20
2	555	759	91:9	165	90:10	49	15
3	590	779	89:11	158	92:8	75	7
4	625	492	59:41	477	60:40	69	14
5	670	88	49:51	939	50:50	84	12

Enantiopure (*P*)-DBH was annealed on Ag(111) at various temperatures.

(*M*)- and (*P*)-**DBH** mirror each other as their helicity controls the handedness of the final chiral adsorbates **P1** and **P2**.

Conclusions

We report here on the enantioenriched assembly of prochiral molecules on an achiral substrate that occurred under chemical control. We demonstrated the chirality transfer from a homochiral helical precursor to the enantiofacially adsorbed prochiral flattened product through a cascade of on-surface reactions. We have provided a detailed analysis of the chemical conversions, which include the identification of individual reaction products by means of high-resolution nc-AFM and STM images. Notably, organic–inorganic chiral surfaces were formed that feature a high e.r. between chiral adsorbates (up to 92:8). An unusually high configurational stability is maintained up to 590 K, which prevents racemization below this temperature. We believe that a wider application of the on-surface asymmetric synthesis will open up other possibilities in expressing and controlling chirality (including a generalized planar one) in 2D molecular self-assemblies on achiral surfaces.

Methods

The helically chiral racemic benzo[2,1-*g*:3,4-*g*′]dichrysene *rac*-**DBH** was synthesized using the procedure we developed earlier[28]. The enantiopure (*P*)-**DBH** (>99% e.e.) was obtained by resolving its racemate through HPLC on a chiral Chiralpak IA column. The molecules were evaporated under ultrahigh vacuum (UHV, 3×10^{-10} mbar) from a tantalum crucible at ~570 K onto an atomically clean Ag(111) single-crystal surface at ~350 K. The enantiopurity of (*P*)-**DBH** in the crucible was preserved even after several evaporation cycles under the aforementioned conditions (determined by HPLC on the Chiralpak IA column). The imaging of the individual molecules and their assemblies was performed by high-resolution nc-AFM and STM under UHV at a low temperature (1.2 K) using a commercial microscope (SPECS Surface Nano Analysis) with simultaneous force/current detection capabilities. The submolecular resolution of flat molecules was achieved in the nc-AFM mode with a single Xe-atom-functionalized tip apex[37]. The thermally induced chemical transformations of the *rac*-**DBH** and enantiopure (*P*)-**DBH** as well as the corresponding intermediates deposited on Ag(111) were achieved by annealing the samples in a preparation chamber of the microscope by an electron-beam heater at the respective temperatures (calibrated by an external optical pyrometer). The optimized structures of the molecules in a vacuum, molecular adsorbates on Ag(111) and transition states were calculated by the Gaussian09, QuantumWise Atomistix 10.8 and FHI-AIMS program packages based on *ab initio* DFT (Supplementary Information gives the details). The theoretical AFM images were calculated using an AFM simulator[6].

Received 4 January 2016; accepted 20 September 2016;

References

1. Blackmond, D. G. The origin of biological homochirality. *Cold Spring Harb. Perspect. Biol.* **2,** a002147 (2010).
2. Carreira, E. M. & Kvaerno, L. *Classics in Stereoselective Synthesis* (Wiley-VCH, 2009).
3. Temirov, R., Soubatch, S., Neucheva, O., Lassise, A. C. & Tautz, F. S. A novel method achieving ultra-high geometrical resolution in scanning tunnelling microscopy. *New J. Phys.* **10,** 053012 (2008).

4. Gross, L., Mohn, F., Moll, N., Liljeroth, P. & Meyer, G. The chemical structure of a molecule resolved by atomic force microscopy. *Science* **325,** 1110–1114 (2009).
5. Gross, L. *et al.* Bond-order discrimination by atomic force microscopy. *Science* **337,** 1326–1329 (2012).
6. Hapala, P. *et al.* The mechanism of high-resolution STM/AFM imaging with functionalized tips. *Phys. Rev. B* **90,** 085421 (2014).
7. Gourdon, A. On-surface covalent coupling in ultrahigh vacuum. *Angew. Chem. Int. Ed.* **47,** 6950–6953 (2008).
8. Méndez, J., López, M. F. & Martín-Gago, J. A. On-surface synthesis of cyclic organic molecules. *Chem. Soc. Rev.* **40,** 4578–4590 (2011).
9. Zhang, X., Zeng, Q. & Wang, C. On-surface single molecule synthesis chemistry: a promising bottom-up approach towards functional surfaces. *Nanoscale* **5,** 8269–8287 (2013).
10. de Oteyza, D. G. *et al.* Direct imaging of covalent bond structure in single-molecule chemical reactions. *Science* **340,** 1434–1437 (2013).
11. Pavliček, N. *et al.* On-surface generation and imaging of arynes by atomic force microscopy. *Nat. Chem.* **7,** 623–628 (2015).
12. Demers-Carpentier, V. *et al.* Stereodirection of an α-ketoester at sub-molecular sites on chirally modified Pt(111): heterogeneous asymmetric catalysis. *J. Am. Chem. Soc.* **135,** 9999–10002 (2013).
13. Amabilino, D. B. *Chirality at the Nanoscale* (Wiley-VCH, 2009).
14. Barlow, S. M. & Raval, R. Complex organic molecules at metal surfaces: bonding, organisation and chirality. *Surf. Sci. Rep.* **50,** 201–341 (2003).
15. Ernst, K.-H. Molecular chirality at surfaces. *Phys. Status Solidi B* **249,** 2057–2088 (2012).
16. Eckhardt, C. J. *et al.* Separation of chiral phases in monolayer crystals of racemic amphiphiles. *Nature* **362,** 614–616 (1993).
17. Stöhr, M. *et al.* Self-assembly and two-dimensional spontaneous resolution of cyano-functionalized [7]helicenes on Cu(111). *Angew. Chem. Int. Ed.* **50,** 9982–9986 (2011).
18. Blüm, M.-C., Ćavar, E., Pivetta, M., Patthey, F. & Schneider, W.-D. Conservation of chirality in a hierarchical supramolecular self-assembled structure with pentagonal symmetry. *Angew. Chem. Int. Ed.* **44,** 5334–5337 (2005).
19. Sun, K. *et al.* Chiral pinwheel clusters lacking local point chirality. *Small* **8,** 2078–2082 (2012).
20. Parschau, M. *et al.* Buckybowls on metal surfaces: symmetry mismatch and enantiomorphism of corannulene on Cu(110). *Angew. Chem. Int. Ed.* **46,** 8258–8261 (2007).
21. Fasel, R., Parschau, M. & Ernst, K.-H. Amplification of chirality in two-dimensional enantiomorphous lattices. *Nature* **439,** 449–452 (2006).
22. Haq, S., Liu, N., Humblot, V., Jansen, A. P. J. & Raval, R. Drastic symmetry breaking in supramolecular organization of enantiomerically unbalanced monolayers at surfaces. *Nat. Chem.* **1,** 409–414 (2009).
23. Parschau, M., Romer, S. & Ernst, K.-H. Induction of homochirality in achiral enantiomorphous monolayers. *J. Am. Chem. Soc.* **126,** 15398–15399 (2004).
24. Destoop, I. *et al.* 'Sergeants-and-Corporals' principle in chiral induction at an interface. *Chem. Commun.* **49,** 7477–7479 (2013).
25. Kündig, P. E. *Transition Metal Arene π-Complexes in Organic Synthesis and Catalysis* (Springer, 2004).
26. Dai, L.-X. *et al. Chiral Ferrocenes in Asymmetric Catalysis* (Wiley-VCH, 2010).
27. Gleiter, R. *et al. Modern Cyclophane Chemistry* (Wiley-VCH, 2004).
28. Jančařík, A. *et al.* Rapid access to dibenzohelicenes and their functionalized derivatives. *Angew. Chem. Int. Ed.* **52,** 9970–9975 (2013).
29. Pinardi, A. L. *et al.* Tailored formation of N-doped nanoarchitectures by diffusion-controlled on-surface (cyclo)dehydrogenation of heteroaromatics. *ACS Nano* **7,** 3676–3684 (2013).
30. Pinardi, A. L. *et al.* Sequential formation of N-doped nanohelicenes, nanographenes and nanodomes by surface-assisted chemical (cyclo) dehydrogenation of heteroaromatics. *Chem. Commun.* **50,** 1555–1557 (2014).
31. Seibel, J., Parschau, M. & Ernst, K.-H. Two-dimensional crystallization of enantiopure and racemic heptahelicene on Ag(111) and Au(111). *J. Phys. Chem. C* **118,** 29135–29141 (2014).
32. Seibel, J., Allemann, O., Siegel, J. S. & Ernst, K.-H. Chiral conflict among different helicenes suppresses formation of one enantiomorph in 2D crystallization. *J. Am. Chem. Soc.* **135,** 7434–7437 (2013).
33. Wang, D. Z., Katz, T. J., Golen, J. & Rheingold, A. L. Diels–Alder additions of benzynes within helicene skeletons. *J. Org. Chem.* **69,** 7769–7771 (2004).
34. Groen, M. B., Schadenberg, H. & Wynberg, H. Synthesis and resolution of some heterohelicenes. *J. Org. Chem.* **36,** 2797–2809 (1971).
35. Fuchter, M. J., Weimar, M., Yang, X., Judge, D. K. & White, A. J. P. An unusual oxidative rearrangement of [7]-helicene. *Tetrahedron Lett.* **53,** 1108–1111 (2012).
36. Berger, R. J. F. *et al.* Gold(I) mediated rearrangement of [7]-helicene to give a benzo[*cd*]pyrenium cation embedded in a chiral framework. *Chem. Commun.* **50,** 5251–5253 (2014).
37. Kichin, G., Weiss, C., Wagner, C., Tautz, F. S. & Temirov, R. Single molecule and single atom sensors for atomic resolution imaging of chemically complex surfaces. *J. Am. Chem. Soc.* **133,** 16847–16851 (2011).

Acknowledgements

This work was financially supported by a Czech Science Foundation grant (14-29667S, 14-16963J) and by the Institute of Organic Chemistry and Biochemistry, Czech Academy of Sciences (RVO: 61388963).

Author contributions

P.J. and I.S. conceived the project and designed the experiments. O.S. and M.Š. performed and analysed the SPM experiments. A.J. synthesized racemic DBH, and J.R. resolved the racemic DBH into enantiomers. J.V.C., J.V., K.K. and P.J. performed theoretical calculations and interpreted their results. I.S. and I.G.S. interpreted the chemical transformations. P.J., O.S., M.Š., I.S. and I.G.S. co-wrote the paper. All the authors discussed the results and commented on the manuscript.

Additional information

Supplementary information and chemical compound information are available in the online version of the paper. Reprints and permissions information is available online at www.nature.com/reprints. Correspondence and requests for materials should be addressed to P.J. and I.S.

Competing financial interests

The authors declare no competing financial interests.

PHYSICAL REVIEW B **95**, 045407 (2017)

Principles and simulations of high-resolution STM imaging with a flexible tip apex

Ondrej Krejčí,[1,2,*] Prokop Hapala,[1] Martin Ondráček,[1] and Pavel Jelínek[1,3]
[1]*Institute of Physics of the Czech Academy of Sciences, v.v.i., Cukrovarnická 10, 162 00 Prague, Czech Republic*
[2]*Charles University in Prague, Faculty of Mathematics and Physics, Department of Surface and Plasma Science, V Holešovičkách 2, 180 00 Prague, Czech Republic*
[3]*Donostia International Physics Center (DIPC), Paseo Manuel Lardizabal 4, E-20018 San Sebastian, Spain*

(Received 30 September 2016; published 6 January 2017)

We present a robust but still efficient simulation approach for high-resolution scanning tunneling microscopy (STM) with a flexible tip apex showing sharp submolecular features. The approach takes into account the electronic structure of the sample and tip as well as relaxation of the tip apex. We validate our model by achieving good agreement with various experimental images which allows us to explain the origin of several observed features. Namely, we have found that the high-resolution STM mechanism consists of standard STM imaging, convolving electronic states of the sample and the tip apex orbital structure, with the contrast heavily distorted by the relaxation of the flexible apex caused by interaction with the substrate.

DOI: 10.1103/PhysRevB.95.045407

I. INTRODUCTION

Both scanning tunneling microscopy (STM) [1] and atomic force microscopy (AFM) [2] have demonstrated the capability to achieve submolecular resolution with a properly functionalized tip apex [3,4]. The unprecedented spatial resolution has advanced the characterization of atomic clusters [5], single molecules [6–8], their assemblies [9,10], and mutual interactions [11,12], as well as the understanding of on-surface chemical reactions [13,14] including the identification of intermediate and final products [15,16].

The origin of submolecular AFM contrast is well established [9,17–19]. In general, the sharp submolecular contrast results from a lateral bending of a flexible tip apex [in our approach represented by a probe particle [18] (PP)]. This bending is caused by a lateral force acting on the tip apex, which results from an interplay between the repulsive Pauli, attractive van der Waals', and electrostatic forces [8]. Sharp edges representing apparent bonds in AFM images [6,20] are the consequence of a discontinuity in the lateral bending of the flexible apex above ridge lines of the potential energy landscape, which are typically located above atoms or bonds [9,18,21].

In principle, high-resolution STM (HR-STM) imaging represents an experimentally less demanding way to achieve submolecular contrast compared to AFM. Furthermore, it provides information about the electronic structure, in addition to the physical structure, of the inspected molecules. Thus, information provided by STM is, in principle, superior to AFM. However, a detailed understanding of the HR-STM imaging mechanism is still missing [18,22,23], impeding its wider proliferation.

Previously, we demonstrated [18,24] that the relaxation of the flexible PP attached to the tip can partially explain the submolecular contrast observed not only in AFM, but also in STM and inelastic electron tunneling spectroscopy (IETS) [25] images . However, the original STM model [18] completely neglects the electronic structure in the description of the tunneling process between tip and sample. The fact that such a crude tunneling model was able to reproduce to some extent the sharp features visible in HR-STM experiments further emphasizes the importance of accounting for the tip apex relaxation in the close-distance regime. On the other hand, numerous HR-STM experiments [1,23,26] indicate that the submolecular contrast depends very much on various experimental details—such as the bias voltage, the substrate, or the microscopic structure of the STM tip apex. Thus, it is evident that the electronic structure has to be included in the correct description of HR-STM imaging.

Traditional STM simulation methods are based on either a nonperturbative approach [27–29] or a perturbative approach (e.g., in Ref. [30]). The latter is only valid when the tip and sample remain out of physical contact [31]. It frequently uses the Bardeen approach [32] and subsequent approximations derived by Chen [33–35] or Tersoff and Hamann [36] (TH). Importantly, the STM methods were devised for surfaces of solid-state materials with a rigid tip apex. Thus they do not take into account any tip apex relaxation, which is fundamental for the understanding of the submolecular contrast with functionalized tips.

In this work, we present an efficient STM model, which takes into account both the PP relaxation as well as electronic wave functions of tip and sample. We will show that this model (hereafter referred to as PP-STM) [37] is able to explain experimentally observed features, which could not be properly reproduced with either the original simple model [18] or traditional STM methods.

II. METHODS

A. Description of the PP-STM model

1. General description of the tunneling process

High-resolution AFM/STM images with functionalized tips are typically acquired at very close distances where repulsive Pauli forces dominate. Therefore, the influence of tip proximity can substantially affect the tunneling barrier [31]. Nevertheless, it has been shown [12] that the tunneling barrier is preserved even in the repulsive regime, due to the presence

---

[*] Corresponding author: krejcio@fzu.cz

of a low-reactivity functionalized tip apex, such as CO or Xe. Consequently, the perturbative approach describing the tunneling processes still remains valid.

Thus, for a description of the tunneling, we make use of Bardeen tunneling theory [32,34], in which we compose the overall tunneling of contributions from individual eigenstates of the tip T and sample S. Here we write the formula in atomic units ($e = m_e = \hbar = 1$),

$$I = 4\pi \int_0^V \sum_T \sum_S \rho_T(E_F - V + \nu)\rho_S(E_F + \nu)|M_{TS}|^2 d\nu, \tag{1}$$

where E_F and V are the Fermi level and applied sample bias voltage, respectively; ρ_S and ρ_T stand for the density of states (DOS) of sample and tip, respectively, at the corresponding energy. Finally, M_{TS} represents the tunneling matrix elements between the states T and S [32,34]. In our method, we consider both tip DOS ρ_T and the tunneling matrix elements M_{TS} to be energetically independent. The conductance G at sample bias voltage V can be simply expressed from Eq. (1),

$$G(V) \equiv \frac{dI}{dV}(V) = 4\pi \sum_T \sum_S \rho_T \rho_S(E_F + V)|M_{TS}|^2. \tag{2}$$

The summations in both Eqs. (1) and (2) go across the eigenstates of tip T and sample S, which are involved in the tunneling process at the given energy, as shown in Fig. 1. Next, we will discuss separately the DOS of the sample (ρ_S) and tip (ρ_T), together with tunneling matrix elements M_{TS}.

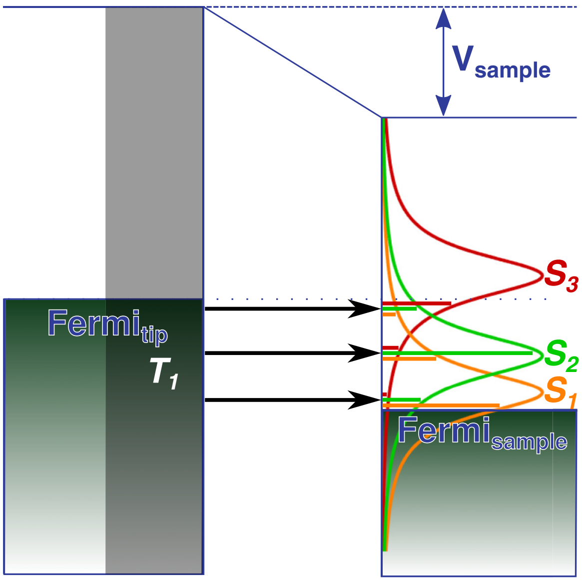

FIG. 1. Schematic illustration of the current calculations: One state of the tip T_1 and three states of sample S_1–S_3 contribute to the current only. The state of the tip T_1 has constant density, while the states of the sample have some Lorentzian broadening around their eigenenergies. The contributions to the tunneling coming from each state of the sample at different energies are illustrated by the full bars on the sample side. The state S_3 contributes to the tunneling, even though the state itself is above the tunneling window. However, its tail gives significant contribution nearby to the upper edge of the tunneling window. In the calculations, the contributions are multiplied by the square of the tunneling matrix elements, $|M_{TS}|^2$.

2. *Density of states of tip ρ_T*

In our approach, the flexible tip is approximated by the last atom of the relaxing tip apex, which is represented by the PP [18,24]. The positions of the tilting PP are precalculated by a PP-AFM code [18,24], as discussed in Sec. III.

In principle, the DOS ρ_T of the tip apex could be obtained from a density functional theory (DFT) calculation for a given tip model. The DOS of the apex can depend on the atomic and chemical structure of both the flexible frontier atom/molecule and a metallic tip base. But typically the precise structure of the metallic tip base in experiments is unknown.

Therefore, we opt for a different strategy, where the tip electronic structure is described by separate s, p_x, p_y, and p_z orbitals located on the PP. The DOS corresponding to each of these orbitals is assumed to be energetically independent. Each of these PP orbitals provides a separate tunneling channel between the PP and sample. We attribute to each DOS of the PP orbital ρ_T a weight between 0 and 1. This allows us to easily analyze the impact of each PP orbital on the calculated STM images and to find the best agreement with experimental evidence. We should note that in the present version, the orbitals on the PP do not tilt with the relaxing PP.

In the case of a weakly bound tip apex (e.g., a Xe atom), additional tunneling can appear—both between the sample and the PP, as expected, as well as between the PP and tip [18]. Here we consider only the tunneling between the PP and the sample. The validity of this approach is supported by good agreement with experimental evidence, as discussed in Sec. III. However, we cannot rule out that in some cases, the second tunneling can further modulate the calculated signal.

3. *Density of states of sample ρ_S*

The DOS of the sample ρ_S for given eigenstate S is represented by a Lorentzian function,

$$\rho_S(V;\eta) = \frac{1}{2\pi} \frac{\eta}{(\varepsilon_S - V)^2 + \eta^2}, \tag{3}$$

where ε_S is the eigenenergy of states S, which is obtained from the total-energy DFT calculations of the sample structure. The η is a broadening factor typically ~0.1 eV.

The total-energy DFT calculations of the sample can be carried out with different codes based on the linear combination of atomic orbitals (LCAO) formalism, for consistency with the formalism in which the tunneling matrix M_{TS} is represented (see discussion later). At the moment, three LCAO DFT codes can be used for creation of input files for the PP-STM code: FIREBALL [38], GPAW [39,40] in LCAO mode [41], and FHI-AIMS [42], but other codes could be easily adapted as well.

4. *Tunneling matrix elements M_{TS}*

The tunneling matrix elements in our approach are approximated by the Chen rules [33,34]. The matrix elements M_{TS} derived in the LCAO formalism can be composed of contributions from separate atoms a (of the sample),

$$M_{TS} = \sum_{a\in\text{atoms of sample}} \frac{2\pi}{\kappa} T_{Ta}^{\text{Chen}}, \tag{4}$$

where the decay constant $\kappa = \sqrt{2W}$ is given by the work function of the sample W [33,34]. The hopping element T_{Ta}^{Chen} represents the contribution from a single atom a derived from the Chen's rules, depending on the corresponding symmetry of the PP orbital T [33,34],

$$T_{Ta}^{\text{Chen}} = \sum_{\alpha\in\text{atom orbitals}} \begin{cases} C_s\phi_\alpha(\vec{r}_a) & \text{if } T \text{ is } s \\ C_p\frac{\partial}{\partial\gamma}\phi_\alpha(\vec{r}_a) & \text{if } T \text{ is } p_\gamma, \end{cases} \tag{5}$$

where $\gamma \in \{x,y,z\}$ and $\vec{r}_a = \vec{r}_a^{\,\text{sample}} - \vec{R}^{\text{PP}}$. Vector $\vec{r}_a^{\,\text{sample}}$ stands for positions of atoms of the sample and $\vec{R}^{\text{PP}}$ is the position of the PP (tip). The constants C_s and C_p are set to $C_s = 1$ and $C_p = \frac{\sqrt{3}}{\kappa}$ according to a derivation shown in Appendix A. We reconstruct the pseudoatom orbital's wave function $\phi_\alpha(\vec{r}_a)$ from the LCAO coefficients of the DFT calculations, standard (real number) spherical harmonics, and a radial part. The radial part is, for simplicity, approximated by a single exponential, given by the characteristic decay length constant κ, which is directly related to the work function of the sample. Here the exponential form ensures the correct decay of the wave function from surface to vacuum [36] and it is assumed to be the same for all atoms of the sample:

$$\phi_\alpha = 2\kappa^{3/2} C_a \exp(-\kappa|\vec{r}_a|) \times \begin{cases} \frac{1}{\sqrt{4\pi}} c^{\text{LCAO}}_{S,a,s} & \text{if } \alpha \text{ is } s \\ \frac{\sqrt{3}}{\sqrt{4\pi}} \frac{y_a}{|\vec{r}_a|} c^{\text{LCAO}}_{S,a,p_y} & \text{if } \alpha \text{ is } p_y \\ \frac{\sqrt{3}}{\sqrt{4\pi}} \frac{z_a}{|\vec{r}_a|} c^{\text{LCAO}}_{S,a,p_z} & \text{if } \alpha \text{ is } p_z \\ \frac{\sqrt{3}}{\sqrt{4\pi}} \frac{x_a}{|\vec{r}_a|} c^{\text{LCAO}}_{S,a,p_x} & \text{if } \alpha \text{ is } p_x, \end{cases} \tag{6}$$

where x_a, y_a, and z_a are Cartesian components of the vector $\vec{r}_a$. The constants $c^{\text{LCAO}}_{S,a,\alpha}$ represent LCAO coefficients of the sample's state S, atom a, and atomic orbital α obtained from the DFT calculations. Since the PP-STM code is made for the calculation of current (or conductivity) flowing from/to adsorbed organic molecules, we consider for simplicity only the valence s and p sample atom orbitals as orbitals α in this work. But the extension of the PP-STM methods including d and f electrons can be done in a straightforward manner.

Finally, we introduced a constant C_a in Eq. (6) in order to have the possibility of changing the amplitude of the atomic tunneling hoppings T_{Ta}^{Chen}. Therefore, we refer to it as the amplitude constant. We typically assume the same amplitude constant ($C_a = 1$) for all atoms of the sample. This approximation of the hoppings gives us good agreement with experiments for two systems—the perylenetetracarboxylic dyanhydride (PTCDA) molecule adsorbed on Au(111) and Ag(111) (see Sec. III A and III B). However, in the case of strongly polarized 1,5,9-trioxo-13-azatriangulene (TOAT) adsorbed on Cu(111), the amplitude of the exponential can be modified by a variation of a tunneling barrier above different atoms of the sample. We discuss this in detail in Sec. III C.

The examples of the fully expanded atomic hoppings T_{Ta}^{Chen} and the matrix elements M_{TS} are shown in Appendix B.

B. Details of DFT calculations

1. PTCDA/Au(111)

We based a slab representing experimentally observed herringbone reconstruction of PTCDA molecules on Au(111) [Fig. 2(a)] on the geometry described by Martínez *et al.* [43]. The Au(111) slab was composed of three layers with Au lattice constant 4.18 and 30 Å of vacuum above it. The topmost golden layer together with the molecular layer were optimized by means of VASP DFT code [44]. For the optimization of the geometry, a GGA-PW91 functional [45], ultrasoft pseudopotentials [46], and Grimme description of van der Waals interactions [47] were applied. The energy cutoff of 396 eV was used for the plane-wave basis set. The force criterion for the differences of the total energy between the optimization steps was set to 10^{-5} eV.

The calculation of the LCAO coefficients was performed with FIREBALL [38] code, using the local density approximation (LDA) functional calculated on a grid with energy cutoff of 300 eV. The Brillouin zone was represented by a Γ point only. The valence basis set and radial cuts for the localized orbitals are shown in Table I of Appendix C. In order to better describe the states of the substrate with Γ point, a 2 × 2 supercell was used for these calculations [shown in Fig. 3(a)]. The DOS projected on the PTCDA molecules is shown in Fig. 3(b).

2. PTCDA/Ag(111)

The geometry of experimentally observed herringbone reconstruction of PTCDA/Ag(111) [Figs. 4(a) and 4(b)] was constructed according to Rohlfing *et al.* [48]. The Ag(111) slab was comprised of three nonrelaxed layers of Ag, with lattice constant 4.09 Å. 30 Å of vacuum above the slab was used in the three-dimensional (3D) periodic boundary conditions. The molecular layer located 3 Å above the substrate was not relaxed.

The LCAO coefficients were also calculated with the FIREBALL code and the same parameters (2 × 2 supercell with Γ point and basis in Table I in Appendix C) as described above for the PTCDA/Au(111). The supercell together with the DOS projected on the molecules are shown in Figs. 3(c) and 3(d), respectively. The Hartree potential used for the PP-AFM calculations was also computed by the FIREBALL code.

3. TOAT/Cu(111)

For DFT calculations of the TOAT molecule on Cu(111), we make use of a geometry obtained with cluster calculations in Ref. [49] that describes the most often observed configuration of the molecule on the surface. The almost flat molecule sits 3.3 Å above the copper layer with oxygens being placed 0.15 Å closer to the substrate [49]. The original small Cu cluster under the molecule was expanded to 91 Cu atoms [shown in Fig. 5(a)] to provide a better description of the substrate. This bigger cluster was used for the calculations of the LCAO coefficients to describe a molecule adsorbed far from other molecules. These calculations were performed with the GPAW code [39–41] in order to show that different codes could be adapted for the PP-STM calculations. The calculations were done with the LDA functional in the LCAO mode and the default basis set. The DOS projected only on the molecule from the GPAW is shown in Fig. 5(b).

The Hartree potential, used for the PP-AFM calculations and for the study of the element-dependent tunneling barrier discussed in Sec. III C, was taken from the original DFT calculations [49]. The shape of the Hartree potential above different atoms of the adsorbed TOAT molecule is shown in Fig. 5(c).

C. PP-AFM calculations

The PP-AFM simulations were done with the PP model described in [18,24]. The calculation of the Lennard-Jones (LJ) force field were done with default LJ parameters [18] (taken from the optimized potential for liquid simulations (OPLS) force field [50]). For these calculations, only the topmost atoms—atoms of the adsorbed molecules—contributed to the LJ force field. The Xe atom on the tip apex was represented by the PP with Xe LJ parameters, while the CO molecule was represented only by oxygen LJ parameters. If the tip apex is charged, the charge Q is represented by a Gaussian cloud with its FWHM of 0.71 Å located on the PP [24]. The PP is positioned 4 Å below the last metal tip atom. The height scale used in the following text denotes the height of the PP above the molecule before relaxation. After the relaxation, the PP can become up to 0.14 Å higher, especially at very close distance scans, where the PP relaxes a lot. This height scale differs from that in Refs. [8,18,24,49].

1. PTCDA/Au(111)

The PP position calculations of PTCDA/Au(111) were done with the default spring stiffness K of 0.5 N/m. In these calculations, no electrostatics were used. The PP was placed 3.2 Å above the molecule for the PTCDA/Au(111) close-distance scan simulations.

2. PTCDA/Ag(111)

The PP-AFM computations were done with the PP parameters that were fitted in Ref. [8] for the set obtained with a positively charged Xe tip: spring stiffness $K = 0.2$ N/m and charge $Q = 0.3$ elementary charge (e). The far- and close-distance scans were calculated with the PP being placed 4.3 and 3.7 Å above the molecule, respectively.

3. TOAT/Cu(111)

The spring stiffness K and the charge Q were set according to the findings in Ref. [8] in the PP-AFM calculations. Namely, they were $K = 0.24$ N/m, $Q = +0.3$ e for the Xe tip simulations, and $K = 0.24$ N/m, $Q = 0.0$ e for the CO tip simulations. For the far-distance Xe tip scan, we positioned the PP 4.9 Å above the molecule, while for the close-distance scan, we positioned the PP 3.5 Å above the molecule. The close-distance scan obtained with the CO tip was simulated with the PP being placed 2.9 Å above the molecule.

III. RESULTS AND DISCUSSION

In what follows, we will examine our approach by comparison with experimental HR-STM images obtained above three different systems: PTCDA molecule adsorbed on Au(111) [43,51] and Ag(111) [8,48] surfaces and TOAT molecule adsorbed on Cu(111) surfaces [49]. The experimental measurements were done in a constant-height STM mode with very low applied bias voltage or in a constant-height dI/dV mode. Since the experimental images acquired with very low bias voltage can be seen as dI/dV maps, all simulated STM images were calculated as constant-height dI/dV maps at a particular energy.

A. PTCDA/Au(111)

Figure 2(a) shows the experimental dI/dV map of PTCDA/Au(111) acquired with a CO-terminated tip at the energy corresponding to the highest occupied molecular orbital (HOMO) of PTCDA [51]. The molecular skeleton is rendered by the characteristic sharp edges, with a pronounced depression of the dI/dV signal located in the central part of the molecule. To disentangle the effect of the electronic structure and the PP relaxation, we first calculated a dI/dV map at the energy of the HOMO without the PP relaxation at a close tip-sample distance; see Fig. 2(b). The combination of the HOMO orbital [shown in the inset of Fig. 2(b)] with p_x and p_y orbitals on the fixed PP transforms the original 12 lobes of the orbital into five stripes at each side of the molecule and four squares in the middle of it. It is noteworthy that unlike the TH, our approach takes into account the cancellation of an STM signal, due to interference effects [35,52,53], that plays an important role in the formation of the STM signal. For example, the destructive interference takes place in the middle of the molecule, where the different phases of the sample and tip orbitals lead to a cancellation of the calculated signal. However, the calculated STM image with fixed PP [Fig. 2(b)] lacks sharp edges and overall agreement with the experimental counterpart is poor.

In the next step, we perform STM simulations including the PP relaxation with the same tip-sample distance and energy; see Fig. 2(c). The impact of the PP relaxation is substantial and the resulting STM image agrees very well with the experimental evidence; compare Fig. 2(a) with 2(c). Namely, the PP relaxations distort the smooth signal giving rise to the sharp edges above the potential ridges. The effect of the relaxation is more clearly pronounced on a comparison of line profiles taken above the center of the molecule; see Fig. 2(d). When the PP is located above a central hexagon, it relaxes towards its center to minimize the interaction energy [positions of the PP are shown in Fig. 2(e)]. Therefore, the signal taken above the central hexagon is almost constant. The sharp edges are also visible on the image obtained with an s orbital on the relaxing PP [Fig. 2(f)]; however, this simulation does not match well with the experimental image. Conversely, the very good agreement between the image simulated with p_x and p_y orbitals on the PP [Fig. 2(c)] and the experimental image obtained with a CO tip in the dI/dV mode [Fig. 2(a)] indicates that the electronic structure of the

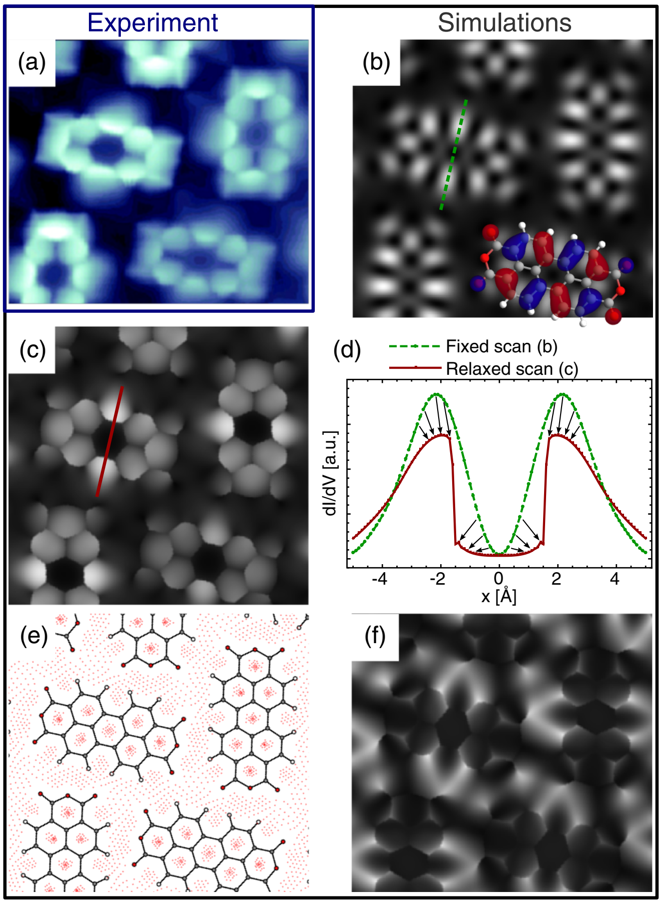

FIG. 2. Comparison between experimental and theoretical STM images calculated with rigid and flexible tip apex. (a) Experimental constant-height HR-STM dI/dV figure of PTCDA/Au(111) obtained with CO tip at $V_{\text{bias}} = -1.6$ V with respect to the sample [51]. (b),(c) Constant-height dI/dV simulations of PTCDA/Au(111) at the energy of HOMO of PTCDA obtained via our PP-STM code using p_x and p_y orbitals on the probe particle (PP) originally placed 3.2 Å above the molecule, with the (b) fixed and (c) relaxed PP, respectively. (d) Comparison of line profiles, taken above centers of PTCDA molecules as indicated by (b) the green dashed line for fixed PP and (c) the red full line for relaxed PP. The arrows indicate the changes in the dI/dV signal given by the PP relaxations. (e) Positions of the relaxed PP, indicated by red dots, when (c) and (f) were simulated. (f) The same scan as (c), but with s orbital on the PP. PP parameters: $K = 0.5$ N/m. All dI/dV scans are done above the area of 25 × 25 Å.

CO tip in this experiment can be well described with p_x and p_y orbitals.

The appearance of sharp edges and the main part of the STM (dI/dV) contrast depends on the PP deviations, and the k stiffness is almost arbitrary—for lower stiffnesses, the deviations appear at higher z positions of tip, and the other way around. Since our main purpose was to show the general mechanism of the HR-STM imaging, we did not try to estimate the stiffness from the comparison with various PP-STM simulations proceeded with different lateral stiffnesses.

It is noteworthy that the PP-STM represents a very efficient method, as the calculated STM images shown in Fig. 2(c), including about 1200 atoms, take only 1 hour on a standard workstation computer.

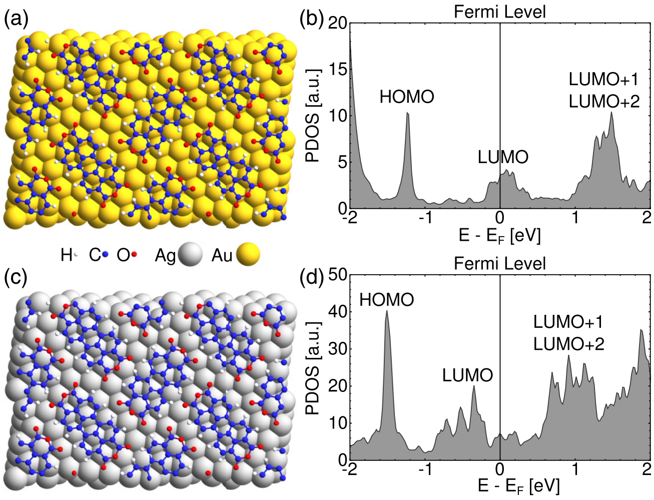

FIG. 3. Properties of PTCDA on Au(111) and Ag(111) surface. (a) Geometry of PTCDA molecules adsorbed on a Au(111) surface. (b) Density of states projected on the molecules for the PTCDA/Au(111) system. (c) Geometry of PTCDA molecules adsorbed on Ag(111) surface. (d) Density of states projected on the molecules for the PTCDA/Ag(111) system. The shown 2 × 2 supercells in (a) and (c) were used for calculations of the LCAO coefficients. The colors of the atoms are shown in the inset between (a) and (c).

B. PTCDA/Ag(111)

Figures 4(a) and 4(b) display experimental images of PTCDA molecules adsorbed on an Ag(111) surface obtained with a Xe tip at low sample bias voltage ($V_{\text{bias}} = -2$ mV [8]) in two different tip-sample distances. Figure 4(a) was acquired in a far tip-sample distance, when tip apex relaxation is not expected. The second experimental image [Fig. 4(b)] was obtained at a smaller tip-sample distance, when the sharp edges in both AFM and STM channels begin to appear. More importantly, the Xe tip in this experimental session was found to be positively charged [8].

Figures 4(c) and 4(d) show calculated STM images obtained with the positively charged Xe tip model ($Q = +0.3\ e$) [8], where we considered only an s orbital on the PP. The good agreement between the experimental STM images [Figs. 4(a) and 4(b)] and their theoretical counterparts [Figs. 4(c) and 4(d)] validates our approach for both far and close tip-sample distances. While in the far-distance regime, the STM contrast is exclusively driven by the electronic structure of both tip and sample, in the close-distance regime the distinctive sharp edges [Figs. 4(b) and 4(d)] coincide with the edges in the HR-AFM image [8]. The positive charge located on the tip apex diminishes the apparent size of the anhydride groups at the edge of the PTCDA molecules in both STM and AFM [8]. This observation confirms that HR-STM images can potentially also be used for an analysis of the electrostatic field [8].

In this case, we were not able to reproduce the experimental contrast considering only freestanding molecule states. That is in contrast to the PTCDA/Au(111) system, where the

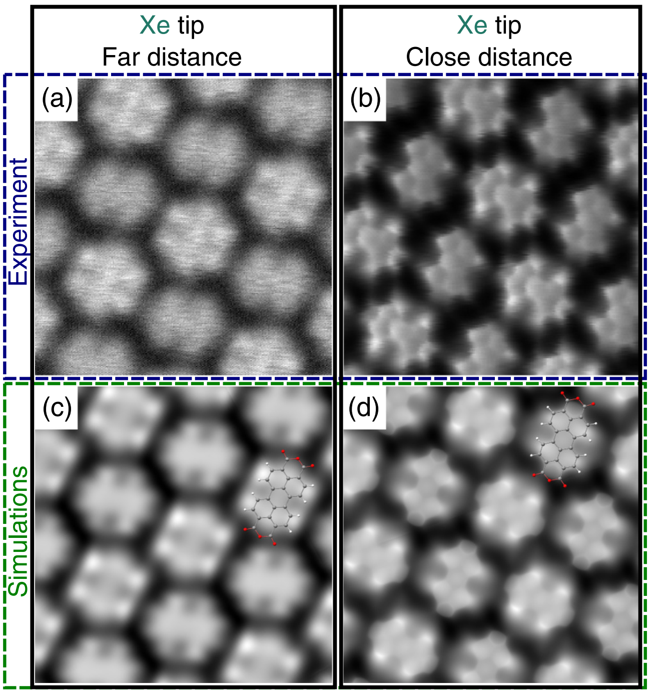

FIG. 4. Comparison of the PP-STM model with experiment—PTCDA/Ag(111)—for different heights of the tip. (a),(b) Constant-height HR-STM obtained with Xe tip and $V_{\text{bias}} = -2$ mV in (a) far and (b) close tip-sample distances, respectively. (c),(d) Simulated PP-STM (dI/dV) images with s orbital on the PP, which is placed (c) 4.3 Å and (d) 3.7 Å above the molecule. The simulation energy is +0.1 eV above the Fermi level. PP parameters: $Q = +0.3\ e$ and $K = 0.2$ N/m. All figures show area 39 × 39 Å.

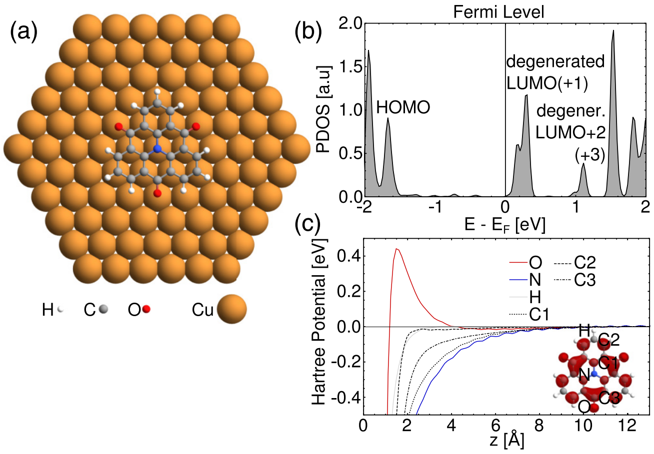

FIG. 5. Properties of TOAT molecule on Cu(111) surface. (a) Geometry of a single molecule adsorbed on a Cu(111) surface. Cluster calculations were used to describe an isolated molecule on the surface. (b) Density of states projected on the molecule for the TOAT/Cu(111) system. (c) Hartree potential profiles taken above the atoms of the molecule. The selected atoms are depicted in the inset, in the right bottom corner. The Hartree potential was taken from original calculations in Ref. [49].

molecular HOMO state was intrinsic to the STM signal. Here the role of the Ag substrate is very important. The simulated images were obtained at energy −0.1 eV below the Fermi level, where the interface states originating from hybridization of the lowest unoccupied molecular orbital (LUMO) with the metallic substrate are located; see Fig. 3(b).

C. TOAT/Cu(111)

In the last example, we will demonstrate not only that other molecules can be simulated, but also that the contrast difference between Xe and CO functionalized tips can be captured by our simulations. We will examine STM images of TOAT molecules deposited on Cu(111) surfaces, which has a large internal charge transfer due to the presence of an N atom in the center and three O atoms on the periphery of the molecule [8]. Figures 6(a) and 6(b) show STM images obtained with a Xe tip in the far- and close-distance regimes, while Fig. 6(c) was acquired with a CO tip in the close-distance regime [49]. We see that the STM contrast obtained in the close-distance regime with Xe and CO tips is quite different.

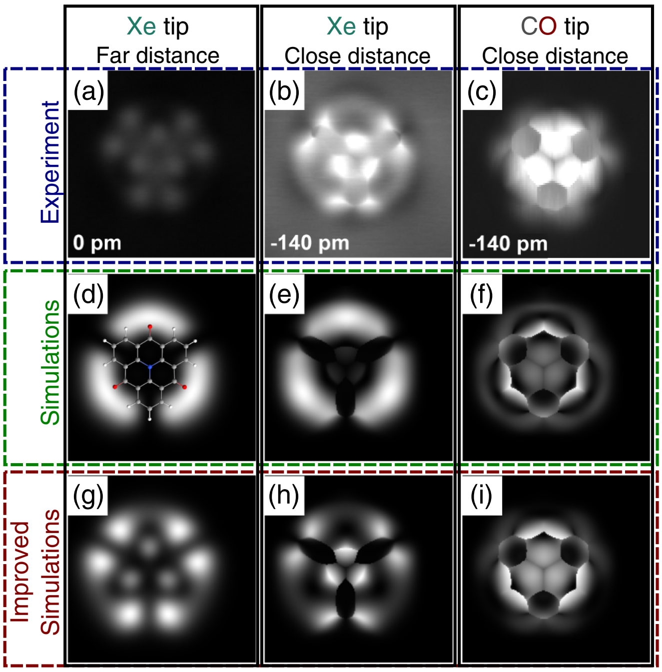

FIG. 6. Comparison of the PP-STM model with experiment—TOAT/Cu(111)—for different tips and heights. (a)–(c) Experimental constant-height HR-STM images of a single TOAT molecule adsorbed on Cu(111) [49], obtained with Xe tip at $V_{\text{bias}} = 200$ mV in (a) large tip-sample distance and (b) tip-sample distance lowered by 1.40 Å. (c) A HR-STM image obtained with a CO tip with small tip-sample distance at $V_{\text{bias}} = 100$ mV. (d),(e) PP-STM simulations at energy +0.2 eV above the Fermi level, with s orbital on the PP ($K = 0.24$ N/m; $Q = +0.3\ e$) for PP height (d) 4.9 Å and (e) 3.5 Å above the molecule. (f) PP-STM simulation at energy +0.2 eV above the Fermi level, with p_x and p_y orbitals on the PP ($K = 0.24$ N/m; $Q = 0.0\ e$) at height 2.9 Å above the molecule. (g)–(i) The same PP-STM simulations as (d) and (f), but with C_a constant for oxygen on the sample lowered by a factor of two. The area of all shown figures is 19 × 19 Å.

The impact of the functionalized tips is twofold. First, an additive electrostatic interaction between PP and the strong electric field of the molecule may significantly change the PP relaxation and, consequently, the apparent position of sharp edges [8]. In the previous work [8], we estimated, from the detailed comparison of the experimental and simulated AFM images, an effective charge for Xe and CO to be +0.3 *e* and 0.0 *e*, respectively. Second, the different electronic wave functions of the functional group on a probe may change the STM contrast. In the next analysis, we will describe the wave function of Xe and CO tips by s and p_x,p_y orbitals on the PP, respectively, as they already provided the very good matches in the previous cases of PTCDA molecules.

Figures 6(d) and 6(e) represent calculated STM images for a positively charged Xe tip, while Fig. 6(f) shows a simulated STM image using a neutral CO tip, both at energy +0.2 eV above the Fermi level. The effect of different effective charge can be nicely seen from a different apparent shape of outer benzene rings in the close-distance images [Figs. 6(b) and 6(c)]. Different orbital symmetries of the tip wave function give rise to distinct contrast in the STM images (compare, e.g., different contrast in the central part and on periphery of the molecule). However, overall agreement between the experiment and the simulation is not very good, especially on the periphery of the molecule.

One possible explanation can be related to the more complex electronic structure of the probe. In particular, Gross *et al.* [52] achieved good agreement between STM images acquired with CO tips in the far-distance regime by taking into account the linear combination of s, p_x, and p_y orbitals on the probe. Pavlíček *et al.* [54] claimed that the p and s contributions can depend on the applied bias voltage. However, in our case, the combinations of $s - p$ orbitals do not improve the agreement with the experimental data.

On the other hand, from analysis of the Hartree potential above the adsorbed molecule, we found a local increase of the tunneling barrier above the oxygens due to a negative partial charge on the oxygen [see Fig. 5(c)]. We tried to mimic the variation of the tunneling barrier by lowering the C_a constant for the oxygen atoms by a factor of two. The HR-STM simulations displayed in Figs. 6(g)–6(i) show significant improvements in the match with the experimental figures for both tip functionalizations and for both tip-sample distance regimes.

More rigorous treatment of the C_a constant, by taking into consideration the local variation of the potential barrier height, is left as a subject for further development. Alternatively, the atomic hoppings T_{Ta} from Eq. (5) could be calculated numerically according to a procedure described in Ref. [29]. We would like to emphasize that many other parameters (e.g., chemical and atomic structure of the whole tip apex including metallic base, charges induced due to the applied bias voltage and/or tip-sample proximity [12], and tunneling between the PP and the tip [18]), which are not taken into account in our model, could also play a role in varying the STM contrast. Despite this fact, we found the PP-STM model provides satisfactory agreement with the available experimental data.

IV. CONCLUSION

In conclusion, we have introduced the PP-STM model for simulations of HR-STM images acquired with a flexible tip apex. The PP-STM model takes into account both the relaxation of the probe particle and the tunneling process between electronic states of the sample and the tip. We have employed the Bardeen theory to describe the tunneling process, while the relaxation of the probe particle is described by the mechanistic PP-AFM model [18,24]. We have performed extensive comparison of simulated HR-STM images with experimental evidence to demonstrate the validity and the limits of the PP-STM model. The model sheds more light on the HR-STM mechanism, which consists of the standard STM imaging heavily distorted by the relaxation of the flexible tip apex. We believe that the detailed understanding of the high-resolution mechanism of STM imaging will serve the further proliferation of application of this technique.

ACKNOWLEDGMENTS

We would like to thank R. Temirov [PTCDA/Au(111)], O. Stetsovych and M. Švec [PTCDA/Ag(111)], and J. van der Lit, N. J. van der Heijden, and I. Swart [TOAT/Cu(111)] for providing us with the experimental images and discussion. We would like to thank N. Pavlicek and J. Repp for fruitful discussions. We acknowledge the support by Czech Science Foundation, Grant No. 14-16963J.

APPENDIX A: DERIVATION OF THE C_s AND C_p CONSTANTS

The constants C_s and C_p are not the Chen's constants C_{lm} that in the original paper describe the tip state composed of many atomic orbitals [33]. In our approach, the states of the tip are single atomic orbitals. The constants C_s and C_p are introduced to the PP-STM model to have mirror symmetry between the tip and the sample: For the same atom on the PP and on the sample, it is natural to expect that the tunneling between the s orbital on the tip and the p_z orbital on the sample would give the same contributions as the contribution obtained with the switched orbitals. This can be rewritten as

$$T^{\mathrm{Chen}}_{sa} = T^{\mathrm{Chen}}_{p_z a}, \tag{A1}$$

where, for the left hopping, $c^{\mathrm{LCAO}}_{S,a,s} = c^{\mathrm{LCAO}}_{S,a,p_y} = c^{\mathrm{LCAO}}_{S,a,p_x} = 0$ and $c^{\mathrm{LCAO}}_{S,a,p_z} = 1$, and for the right hopping, $c^{\mathrm{LCAO}}_{S,a,p_y} = c^{\mathrm{LCAO}}_{S,a,p_z} = c^{\mathrm{LCAO}}_{S,a,p_x} = 0$ and $c^{\mathrm{LCAO}}_{S,a,s} = 1$. Now the left hopping can be rewritten according to Eq. (B1) without its zero contributions,

$$T^{\mathrm{Chen}}_{sp_z} = 2\kappa^{3/2} C_s C_a \exp(-\kappa|\vec{r}_a|)\frac{1}{\sqrt{4\pi}}\left[\sqrt{3}\frac{z_a}{|\vec{r}_a|}\right]. \tag{A2}$$

An analogy to Eq. (B2) for the p_z orbital on the tip can be derived from Eqs. (5) and (6). Here we show only the part without the zero contribution necessary for the constants derivation,

$$T^{\rm Chen}_{p_z s} = 2\kappa^{3/2} C_p C_a \exp(-\kappa|\vec{r}_a|)\frac{1}{\sqrt{4\pi}}\frac{1}{|\vec{r}_a|}[z_a\kappa]. \tag{A3}$$

Since we do not require quantitative agreement with experiment and since C_s is arbitrary in the previous consideration, we set it to one ($C_s = 1$). Now, the constant C_p can be enumerated from Eqs. (A2) and (A3),

$$C_p = \frac{\sqrt{3}}{\kappa}. \tag{A4}$$

APPENDIX B: EXPANSION OF TUNNELING MATRIX ELEMENTS M_{TS} AND ATOMIC CONTRIBUTIONS $T^{\rm Chen}_{Ta}$

1. Expansion of atomic contributions $T^{\rm Chen}_{Ta}$

According to Eq. (5), the atomic hoppings $T^{\rm Chen}_{Ta}$ depend on the symmetry of the tip—more precisely on the orbital T localized on the PP. Here we show two examples of fully expanded $T^{\rm Chen}_{Ta}$ hoppings derived from Eqs. (5) and (6) for s and p_y orbital on the PP:

$$T^{\rm Chen}_{sa} = 2\kappa^{3/2} C_s C_a \exp(-\kappa|\vec{r}_a|)\frac{1}{\sqrt{4\pi}}\left[c^{\rm LCAO}_{S,a,s} + \sqrt{3}\frac{y_a}{|\vec{r}_a|}c^{\rm LCAO}_{S,a,p_y} + \sqrt{3}\frac{z_a}{|\vec{r}_a|}c^{\rm LCAO}_{S,a,p_z} + \sqrt{3}\frac{x_a}{|\vec{r}_a|}c^{\rm LCAO}_{S,a,p_x}\right] \tag{B1}$$

and

$$\begin{aligned} T^{\rm Chen}_{p_y a} = {} & 2\kappa^{3/2} C_p C_a \exp(-\kappa|\vec{r}_a|)\frac{1}{\sqrt{4\pi}}\frac{1}{|\vec{r}_a|}\left[y_a\kappa c^{\rm LCAO}_{S,a,s} \right. \\ & + \sqrt{3}\left(\frac{y_a^2}{|\vec{r}_a|^2} + \frac{y_a^2}{|\vec{r}_a|}\kappa - 1\right)c^{\rm LCAO}_{S,a,p_y} \\ & + \sqrt{3}\left(\frac{y_a z_a}{|\vec{r}_a|^2} + \frac{y_a z_a}{|\vec{r}_a|}\kappa\right)c^{\rm LCAO}_{S,a,p_z} \\ & \left. + \sqrt{3}\left(\frac{y_a x_a}{|\vec{r}_a|^2} + \frac{y_a x_a}{|\vec{r}_a|}\kappa\right)c^{\rm LCAO}_{S,a,p_x}\right], \end{aligned} \tag{B2}$$

respectively.

2. Full expansion of M_{sS} for s orbital on PP

$$M_{sS} = \sum_a \sqrt{4\pi\kappa} C_a C_s \exp(-\kappa|\vec{r}_a|)\left[c^{\rm LCAO}_{S,a,s} + \sqrt{3}\frac{y_a}{|\vec{r}_a|}c^{\rm LCAO}_{S,a,p_y} + \sqrt{3}\frac{z_a}{|\vec{r}_a|}c^{\rm LCAO}_{S,a,p_z} + \sqrt{3}\frac{x_a}{|\vec{r}_a|}c^{\rm LCAO}_{S,a,p_x}\right]. \tag{B3}$$

3. Full expansion of M_{p_yS} for p_y orbital on PP

$$\begin{aligned} M_{p_yS} = {} & \sum_a \sqrt{4\pi\kappa} C_a C_p \exp(-\kappa|\vec{r}_a|)\frac{1}{|\vec{r}_a|}\left[y_a\kappa c^{\rm LCAO}_{S,a,s} \right. \\ & + \sqrt{3}\left(\frac{y_a^2}{|\vec{r}_a|^2} + \frac{y_a^2}{|\vec{r}_a|}\kappa - 1\right)c^{\rm LCAO}_{S,a,p_y} \\ & + \sqrt{3}\left(\frac{y_a z_a}{|\vec{r}_a|^2} + \frac{y_a z_a}{|\vec{r}_a|}\kappa\right)c^{\rm LCAO}_{S,a,p_z} \\ & \left. + \sqrt{3}\left(\frac{y_a x_a}{|\vec{r}_a|^2} + \frac{y_a x_a}{|\vec{r}_a|}\kappa\right)c^{\rm LCAO}_{S,a,p_x}\right]. \end{aligned} \tag{B4}$$

APPENDIX C: TABLE OF RADIAL CUTS FOR FIREBALL BASIS SET

The radial cut off radii of numerical basis set used in the PP-STM simulations are listed in Table I.

TABLE I. The radial cuts for the basis set used in the FIREBALL calculations. a_b stands for the Bohr radius. * marks an excited orbital.

Atom	Orbital	Radial cut (a_b)	Atom	Orbital	Radial cut (a_b)
H	s	4.0	Ag	s	4.5
	s*	4.0		p	5.5
				s*	4.0
C	s	4.5	Au	s	4.5
	p	4.5		p	5.6
	d	5.4		d	4.3
O	s	3.3			
	p	3.8			
	s*	3.3			
	p*	3.8			

---

[1] R. Temirov, S. Soubatch, O. Neucheva, A. C. Lassise, and F. S. Tautz, New J. Phys. **10**, 053012 (2008).

[2] L. Gross, F. Mohn, N. Moll, P. Liljeroth, and G. Meyer, Science **325**, 1110 (2009).

[3] L. Bartels, G. Meyer, K.-H. Rieder, D. Velic, E. Knoesel, A. Hotzel, M. Wolf, and G. Ertl, Phys. Rev. Lett. **80**, 2004 (1998).

[4] F. Mohn, B. Schuler, L. Gross, and G. Meyer, Appl. Phys. Lett. **102**, 073109 (2013).

[5] M. Emmrich, F. Huber, F. Pielmeier, J. Welker, M. Schneiderbauer, T. Hofmann, D. Meuer, S. Polesya, S. Mankovsky, D. Kodderitzsch, H. Ebert, and F. J. Giessibl, Science **348**, 308 (2015).

[6] L. Gross, F. Mohn, N. Moll, B. Schuler, A. Criado, E. Guitián, D. Peña, A. Gourdon, and G. Meyer, Science **337**, 1326 (2012).

[7] F. Albrecht, J. Repp, M. Fleischmann, M. Scheer, M. Ondráček, and P. Jelínek, Phys. Rev. Lett. **115**, 076101 (2015).

[8] P. Hapala, M. Svec, O. Stetsovych, N. J. van der Heijden, M. Ondracek, J. van der Lit, P. Mutombo, I. Swart, and P. Jelínek, Nat. Commun. **7**, 11560 (2016).

[9] S. K. Hämäläinen, N. van der Heijden, J. van der Lit, S. den Hartog, P. Liljeroth, and I. Swart, Phys. Rev. Lett. **113**, 186102 (2014).

[10] S. Kawai, A. Sadeghi, X. Feng, P. Lifen, R. Pawlak, T. Glatzel, A. Willand, A. Orita, J. Otera, S. Goedecker, and E. Meyer, ACS Nano **7**, 9098 (2013).

[11] Z. Sun, M. Boneschanscher, I. Swart, D. Vanmaekelbergh, and P. Liljeroth, Phys. Rev. Lett. **106**, 046104 (2011).

[12] M. Corso, M. Ondracek, C. Lotze, P. Hapala, K. J. Franke, P. Jelinek, and J. I. Pascual, Phys. Rev. Lett. **115**, 136101 (2015).

[13] L. Gross, N. Moll, G. Meyer, R. Ebel, W. M. Abdel-Mageed, and M. Jaspars, Nat. Chem. **2**, 821 (2010).

[14] N. Pavliček, B. Schuler, S. Collazos, N. Moll, D. Pérez, E. Guitián, G. Meyer, D. Peña, and L. Gross, Nat. Chem. **7**, 623 (2015).

[15] D. G. de Oteyza, P. Gorman, Y.-C. Chen, S. Wickenburg, A. Riss, D. J. Mowbray, G. Etkin, Z. Pedramrazi, H.-Z. Tsai, A. Rubio, M. F. Crommie, and F. R. Fischer, Science **340**, 1434 (2013).

[16] B. Schuler, G. Meyer, D. Peña, O. C. Mullins, and L. Gross, J. Am. Chem. Soc. **137**, 9870 (2015).

[17] N. Moll, L. Gross, F. Mohn, A. Curioni, and G. Meyer, New J. Phys. **12**, 125020 (2010).

[18] P. Hapala, G. Kichin, C. Wagner, F. S. Tautz, R. Temirov, and P. Jelínek, Phys. Rev. B **90**, 085421 (2014).

[19] C.-S. Guo, M. A. Van Hove, X. Ren, and Y. Zhao, J. Phys. Chem. C **119**, 1483 (2015).

[20] N. Pavliček, C. Herranz-Lancho, B. Fleury, M. Neu, J. Niedenführ, M. Ruben, and J. Repp, Phys. Status Solidi B **250**, 2424 (2013).

[21] M. P. Boneschanscher, S. K. Hämäläinen, P. Liljeroth, and I. Swart, ACS Nano **8**, 3006 (2014).

[22] J. I. Martínez, E. Abad, C. González, F. Flores, and J. Ortega, Phys. Rev. Lett. **108**, 246102 (2012).

[23] C. Weiss, C. Wagner, C. Kleimann, M. Rohlfing, F. S. Tautz, and R. Temirov, Phys. Rev. Lett. **105**, 086103 (2010).

[24] P. Hapala, R. Temirov, F. S. Tautz, and P. Jelínek, Phys. Rev. Lett. **113**, 226101 (2014).

[25] C. l. Chiang, C. Xu, Z. Han, and W. Ho, Science **344**, 885 (2014).

[26] P. Hapala, M. Ondráček, O. Stetsovych, M. Švec, and P. Jelínek, *Noncontact Atomic Force Microscopy: Vol. 3* (Springer International, Cham, Switzerland, 2015), pp. 29–49.

[27] J. Cerdá, M. A. Van Hove, P. Sautet, and M. Salmeron, Phys. Rev. B **56**, 15885 (1997).

[28] N. Mingo, L. Jurczyszyn, F. J. Garcia-Vidal, R. Saiz-Pardo, P. L. de Andres, F. Flores, S. Y. Wu, and W. More, Phy. Rev. B **54**, 2225 (1996).

[29] J. M. Blanco, F. Flores, and R. Pérez, Prog. Surf. Sci. **81**, 403 (2006).

[30] W. Hofer, Prog. Surf. Sci. **71**, 147 (2003).

[31] J. M. Blanco, C. Gonzalez, P. Jelinek, J. Ortega, F. Flores, and R. Perez, Phys. Rev. B **70**, 085405 (2004).

[32] J. Bardeen, Phys. Rev. Lett. **6**, 57 (1961).

[33] C. J. Chen, Phys. Rev. B **42**, 8841 (1990).

[34] C. J. Chen, *Introduction to Scanning Tunneling Microscopy*, Vol. 2 (Oxford University Press, New York, 2008).

[35] G. Mándi and K. Palotás, Phys. Rev. B **91**, 165406 (2015).

[36] J. Tersoff and D. R. Hamann, Phys. Rev. B **31**, 805 (1985).

[37] https://github.com/ProkopHapala/ProbeParticleModel/tree/PPSTM (unpublished).

[38] J. P. Lewis, P. Jelínek, J. Ortega, A. A. Demkov, D. G. Trabada, B. Haycock, H. Wang, G. Adams, J. K. Tomfohr, E. Abad, H. Wang, and D. A. Drabold, Phys. Status Solidi B **248**, 1989 (2011).

[39] J. J. Mortensen, L. B. Hansen, and K. W. Jacobsen, Phys. Rev. B **71**, 035109 (2005).

[40] J. Enkovaara *et al.*, J. Phys.: Condens. Matter **22**, 253202 (2010).

[41] A. H. Larsen, M. Vanin, J. J. Mortensen, K. S. Thygesen, and K. W. Jacobsen, Phys. Rev. B **80**, 195112 (2009).

[42] V. Blum, R. Gehrke, F. Hanke, P. Havu, V. Havu, X. Ren, K. Reuter, and M. Scheffler, Comput. Phys. Commun. **180**, 2175 (2009).

[43] J. Martínez, E. Abad, F. Flores, J. Ortega, and G. Brocks, Chem. Phys. **390**, 14 (2011).

[44] G. Kresse and J. Furthmüller, Phys. Rev. B **54**, 11169 (1996).

[45] J. P. Perdew, J. A. Chevary, S. H. Vosko, K. A. Jackson, M. R. Pederson, D. J. Singh, and C. Fiolhais, Phys. Rev. B **46**, 6671 (1992).

[46] D. Vanderbilt, Phys. Rev. B **41**, 7892 (1990).

[47] S. Grimme, J. Comput. Chem. **27**, 1787 (2006).

[48] M. Rohlfing, R. Temirov, and F. S. Tautz, Phys. Rev. B **76**, 115421 (2007).

[49] N. J. van der Heijden, P. Hapala, J. A. Rombouts, J. van der Lit, D. Smith, P. Mutombo, M. Švec, P. Jelínek, and I. Swart, ACS Nano **10**, 8517 (2016).

[50] W. L. Jorgensen and J. Tirado-Rives, J. Am. Chem. Soc. **110**, 1657 (1988).

[51] G. Kichin, C. Wagner, F. S. Tautz, and R. Temirov, Phys. Rev. B **87**, 081408 (2013).

[52] L. Gross, N. Moll, F. Mohn, A. Curioni, G. Meyer, F. Hanke, and M. Persson, Phys. Rev. Lett. **107**, 086101 (2011).

[53] M. Telychko, P. Mutombo, M. Ondráček, P. Hapala, F. C. Bocquet, J. Kolorenč, M. Vondráček, P. Jelínek, and M. Švec, ACS Nano **8**, 7318 (2014).

[54] N. Pavliček, I. Swart, J. Niedenführ, G. Meyer, and J. Repp, Phys. Rev. Lett. **110**, 136101 (2013).